The Astrophysical Journal, 961:29 (17pp), 2024 January 20 https://doi.org/10.3847/1538-4357/ad06aa
© 2024. The Author(s). Published by the American Astronomical Society.
OPEN ACCESS

Filamentary Dust Polarization and the Morphology of Neutral Hydrogen Structures

George Halal[1,2], Susan E. Clark[1,2], Ari Cukierman[1,2,3,4], Dominic Beck[1,2,3], and Chao-Lin Kuo[1,2,3]
[1] Department of Physics, Stanford University, Stanford, CA 94305, USA; georgech@stanford.edu
[2] Kavli Institute for Particle Astrophysics and Cosmology (KIPAC), Stanford University, Stanford, CA 94305, USA
[3] SLAC National Accelerator Laboratory, Menlo Park, CA 94025, USA
[4] Department of Physics, California Institute of Technology, Pasadena, CA 91125, USA
Received 2023 June 16; revised 2023 October 21; accepted 2023 October 23; published 2024 January 11

Abstract

Filamentary structures in neutral hydrogen (H I) emission are well aligned with the interstellar magnetic field, so H I emission morphology can be used to construct templates that strongly correlate with measurements of polarized thermal dust emission. We explore how the quantification of filament morphology affects this correlation. We introduce a new implementation of the Rolling Hough Transform (RHT) using spherical harmonic convolutions, which enables efficient quantification of filamentary structure on the sphere. We use this Spherical RHT algorithm along with a Hessian-based method to construct H I-based polarization templates. We discuss improvements to each algorithm relative to similar implementations in the literature and compare their outputs. By exploring the parameter space of filament morphologies with the Spherical RHT, we find that the most informative H I structures for modeling the magnetic field structure are the thinnest resolved filaments. For this reason, we find a $\sim$10% enhancement in the *B*-mode correlation with polarized dust emission with higher-resolution H I observations. We demonstrate that certain interstellar morphologies can produce parity-violating signatures, i.e., nonzero *TB* and *EB*, even under the assumption that filaments are locally aligned with the magnetic field. Finally, we demonstrate that *B* modes from interstellar dust filaments are mostly affected by the topology of the filaments with respect to one another and their relative polarized intensities, whereas *E* modes are mostly sensitive to the shapes of individual filaments.

Unified Astronomy Thesaurus concepts: Interstellar dust (836); Interstellar filaments (842); Milky Way magnetic fields (1057); Neutral hydrogen clouds (1099); Cosmic microwave background radiation (322); Algorithms (1883); Interstellar magnetic fields (845); Interstellar medium (847); Interstellar atomic gas (833); Interstellar phases (850); Galaxy magnetic fields (604); Magnetic fields (994)

1. Motivation

Modeling polarized dust emission is crucial for studying various astrophysical phenomena in the interstellar medium (ISM) and for analyzing the polarization of the cosmic microwave background (CMB). Aspherical rotating dust grains preferentially align their short axes with the local magnetic field, resulting in their thermal emission being linearly polarized (Purcell 1975). Dust polarization thus traces the plane-of-sky magnetic field orientation and is widely used to trace magnetic field structure in the Galaxy (e.g., Han 2017). At large scales and frequencies greater than approximately 70 GHz, polarized dust emission is the predominant polarized CMB foreground (Planck Collaboration et al. 2016a). The accurate modeling and elimination of the dust contribution to CMB polarization measurements are essential to search for an excess polarization signal induced by primordial gravitational waves (Kamionkowski et al. 1997; Seljak & Zaldarriaga 1997; Seljak 1997).

Galactic neutral hydrogen (H I) emission is a tracer of the neutral medium that can be fruitfully compared to the dust distribution. H I and dust trace similar volumes of the diffuse ISM (Boulanger et al. 1996; Lenz et al. 2017). Much of the diffuse H I emission is organized into filamentary structures that show significant alignment with the plane-of-sky magnetic field orientation (Clark et al. 2014, 2015). The spectroscopic nature of H I measurements means that these structures can be studied in 3D, namely as a function of longitude, latitude, and radial velocity with respect to the local standard of rest $v_{\rm lsr}$, i.e., the Doppler-shifted frequency of the 21 cm line (Clark 2018). Furthermore, because H I and broadband thermal dust emission are independently observed, cross correlations between the two are free from correlated telescope systematics. H I data are also not contaminated by the cosmic infrared background (Chiang & Ménard 2019).

Using these insights, Clark & Hensley (2019) developed a model of polarized dust emission based solely on H I measurements. Cross correlations between this dust polarization model and millimeter-wave polarization data have proven useful for characterizing dust properties such as the spectral index (BICEP/Keck Collaboration et al. 2023). Clark & Hensley (2019) used the Rolling Hough Transform (RHT; Clark et al. 2014, 2020) algorithm as a first step for quantifying the orientations of linear dust filaments. The RHT has free parameters that set the scale and shape of the identified filaments. This is ideal for the exploration of different filament morphologies and their polarization effects.

The RHT algorithm runs on images or flat-sky projections of small patches of the sky. It is possible to construct an H I-based polarization template on the full sky by projecting a small patch of the spherical map around each pixel to an image, running the algorithm, and projecting the result back to the sphere, as done in Clark & Hensley (2019) for a single set of parameters. However, this is computationally expensive to perform for

Original content from this work may be used under the terms of the Creative Commons Attribution 4.0 licence. Any further distribution of this work must maintain attribution to the author(s) and the title of the work, journal citation and DOI.

multiple sets of parameters. In this paper, we develop an algorithm for running the RHT directly on the sphere using spherical harmonic convolutions.

Another filament-finding algorithm that can be used to construct polarization templates from H I emission is based on the Hessian matrix (e.g., Cukierman et al. 2023). We explore the advantages and disadvantages of the Hessian-based algorithm relative to the RHT-based algorithm.

The paper is organized as follows. We introduce the dust emission and H I data used in this work in Section 2. We explore how different modifications to the Hessian-based polarization template affect the correlation with polarized dust emission in Section 4. We introduce a spherical convolution version of the RHT in Section 5. We use it to explore the polarization effects of different filament morphologies and how filament-finding algorithms can be used for determining morphologies that produce parity-violating polarization signatures in Section 6. We summarize and conclude in Section 7.

2. Data

2.1. Dust Emission

We make use of two sets of Stokes I, Q, and U Planck data products at 353 GHz provided by the Planck Legacy Archive.[5] The first is the set of Planck `Commander` dust maps with an angular resolution of 5′, constructed by component separation applied to the Planck frequency maps (Planck Collaboration et al. 2020a). The second is the set of 353 GHz maps from Planck data release R3.01 with an angular resolution of 5′ (Planck Collaboration et al. 2020b). While the former is processed to remove emission other than dust, the latter contains contributions from multiple components. We compare these two data products in Section 4.2 and use the `Commander` dust maps for all subsequent analyses. The reported results are insensitive to smoothing the Planck data, so we use them at their native resolution.

For cross-spectrum calculations between these maps and other polarization data products in this paper, we use the full-mission maps. When calculating autospectra of these maps, we compute cross spectra of the half-mission splits to avoid noise bias.

For most of the analysis in this paper, we use the Planck 70% sky fraction Galactic plane mask (Planck Collaboration et al. 2015). However, in Section 4.2, we also employ the 20%, 40%, 60%, and 80% sky fraction Galactic plane masks. The higher the sky fraction, the greater the contribution from lower Galactic latitudes.

2.2. Neutral Hydrogen

For the Galactic neutral hydrogen (H I) emission, we use the H I 4π Survey (HI4PI; HI4PI Collaboration et al. 2016), which has the highest-resolution full-sky measurements of the 21 cm hyperfine transition to date. HI4PI merges data from the Effelsberg–Bonn H I Survey (EBHIS; Winkel et al. 2016) and the Parkes Galactic All-Sky Survey (GASS; McClure-Griffiths et al. 2009) to achieve an angular resolution of 16.′2, a spectral resolution of 1.49 km s^{-1}, and a normalized brightness temperature noise of ∼53 mK for a 1 km s^{-1} velocity channel. We use the publicly available H I intensity data described in Clark & Hensley (2019), binned into velocity channels of equal integrated intensity in each pair of channels moving symmetrically outward from the local standard of rest.

In Section 4.3, we also use H I emission data from the Galactic Arecibo L-Band Feed Array H I Survey (GALFA-H I; Peek et al. 2018), which is higher resolution but only covers ∼32% of the sky. GALFA-H I has an angular resolution of 4.′1, a spectral resolution of 0.184 km s^{-1}, and a normalized brightness temperature noise of 150 mK for a 1 km s^{-1} channel. We also use the publicly available H I intensity data described in Clark & Hensley (2019), binned into velocity channels of equal width of 3.7 km s^{-1}. These maps span the range $1.^\circ5 <$ decl. $< 35.^\circ5$ to avoid telescope scan artifacts at the edges of the Arecibo declination range.

3. H I-based Dust Polarization Prediction

The H I-based polarization templates are constructed by measuring the orientation of linear structures to determine the polarization angle and combining this information with some weighting representing the polarized intensity at different locations in the map. The orientation can be determined by different algorithms applied to the H I intensity maps. In this section, we summarize the two algorithms we use in this paper for polarization angle determination and describe how their outputs are used along with different polarized intensity weighting schemes to construct H I-based polarization templates.

3.1. RHT-based Angle Determination

The RHT is a computer vision algorithm that identifies linear structures and their orientations in images (Clark et al. 2014, 2020). The steps involved in this process are:

1. Unsharp masking, which involves subtracting a version of the map smoothed to a given scale, $\theta_{\rm FWHM}$, from the original map. This step acts as a high-pass filter of the map to remove larger-scale emission.
2. Bit masking, which converts all pixels with negative values to zero and all pixels with positive values to one.
3. Applying the Hough transform (Hough 1962) on a circular window of a given diameter, $D_{\rm W}$, centered on each pixel to quantify the relative intensities of differently oriented linear structures passing through that pixel.
4. Storing only the linear intensities over a certain threshold fraction, Z, of the window diameter. The output is stored as linear intensity as a function of orientation $R(\hat{\boldsymbol{n}}, \theta, \nu)$.

This algorithm, therefore, has three free parameters, $\theta_{\rm FWHM}$, $D_{\rm W}$, and Z, which can be tuned to different values for different applications.

3.2. Hessian-based Angle Determination

Hessian-based filament identification has been applied to different maps, e.g., Planck 353 GHz total intensity maps (Planck Collaboration et al. 2016b, 2016c), HI4PI H I intensity and Planck 857 GHz total intensity maps (Kalberla et al. 2021), Herschel images of molecular clouds (Polychroni et al. 2013), and simulations of the cosmic web (Colombi et al. 2000; Forero-Romero et al. 2009). In this work, we use the version of the Hessian-based filament-finding algorithm described in Cukierman et al. (2023).

The Hessian matrix serves as a tool to determine the orientation of filaments. It contains information about the local second derivatives. A negative curvature indicates the presence

[5] pla.esac.esa.int

of at least one negative Hessian eigenvalue. By examining a map for areas exhibiting negative curvature, we can identify possible filaments.

We apply the Hessian to the H I intensity maps in individual velocity bins I. We work in spherical coordinates with polar angle θ and azimuthal angle ϕ. The local Hessian matrix is given by

$$H \equiv \begin{pmatrix} H_{xx} & H_{xy} \\ H_{yx} & H_{yy} \end{pmatrix}, \tag{1}$$

where

$$H_{xx} = \frac{\partial^2 I}{\partial \theta^2}, \tag{2}$$

$$H_{yy} = \frac{1}{\sin^2\theta}\frac{\partial^2 I}{\partial \phi^2}, \tag{3}$$

$$H_{xy} = H_{yx} = -\frac{1}{\sin\theta}\frac{\partial^2 I}{\partial \phi \partial \theta}. \tag{4}$$

The eigenvalues are

$$\lambda_{\pm} = \frac{1}{2}(H_{xx} + H_{yy} \pm \alpha), \tag{5}$$

where

$$\alpha \equiv \sqrt{(H_{xx} - H_{yy})^2 \quad + \quad 4H_{xy}^2}. \tag{6}$$

For the local curvature to be negative along at least one axis, we require $\lambda_- < 0$. We also require λ_- to be the larger of the two eigenvalues in magnitude such that this negative curvature is the dominant local morphology. In constructing H I-based polarization templates, we define a weighting $w_{\rm H}$ for each pixel at each velocity that is equal to λ_- when the eigenvalues satisfy our two requirements and equal to zero when they do not.

The orientation of the filaments is determined by the local eigenbasis. The polarization angle is determined as

$$\theta_{\rm H} = \arctan\left(\frac{H_{xx} - H_{yy} + \alpha}{2H_{xy}}\right). \tag{7}$$

3.3. H I-based Polarization Template Construction

The polarization angle determined using the RHT and Hessian algorithms can be combined with some weighting representing the local contribution to the H I-based polarized intensity to construct H I-based polarization templates. For instance, Clark & Hensley (2019) normalize the RHT-measured linear intensity $R(\hat{\boldsymbol{n}}, \theta, v)$ over different orientation bins such that

$$\sum_{\theta} R(\hat{\boldsymbol{n}}, \theta, v) = 1. \tag{8}$$

They use the normalized $R(\hat{\boldsymbol{n}}, \theta, v)$ and the H I intensity maps $I_{\rm H\,I}(\hat{\boldsymbol{n}}, v)$ as the weighting to produce Stokes $Q_{\rm RHT}$ and $U_{\rm RHT}$ maps as

$$Q_{\rm RHT}(\hat{\boldsymbol{n}}, v) = I_{\rm H\,I}(\hat{\boldsymbol{n}}, v)\sum_{\theta} R(\hat{\boldsymbol{n}}, \theta, v)\cos 2\theta, \tag{9}$$

$$U_{\rm RHT}(\hat{\boldsymbol{n}}, v) = I_{\rm H\,I}(\hat{\boldsymbol{n}}, v)\sum_{\theta} R(\hat{\boldsymbol{n}}, \theta, v)\sin 2\theta. \tag{10}$$

These maps have the same units (K km s^{-1}) as the intensity maps, $I_{\rm H\,I}(\hat{\boldsymbol{n}}, v)$. To construct the H I-based polarization template, the Stokes parameter maps are integrated over velocity channels as

$$Q_{\rm RHT}(\hat{\boldsymbol{n}}) = \sum_{v} Q_{\rm RHT}(\hat{\boldsymbol{n}}, v), \tag{11}$$

$$U_{\rm RHT}(\hat{\boldsymbol{n}}) = \sum_{v} U_{\rm RHT}(\hat{\boldsymbol{n}}, v). \tag{12}$$

The Hessian-based filament-finding algorithm (hereafter Hessian algorithm), by contrast, uses the local eigenbasis of the Hessian matrix to determine the orientation of linear structures, and the negative eigenvalues to determine the Stokes weighting (Cukierman et al. 2023). See Section 3.2 for details. Equations (9) and (10), therefore, become

$$Q_{\rm H}(\hat{\boldsymbol{n}}, v) = w_{\rm H}(\hat{\boldsymbol{n}}, v)\cos 2\theta_{\rm H}(\hat{\boldsymbol{n}}, v), \tag{13}$$

$$U_{\rm H}(\hat{\boldsymbol{n}}, v) = w_{\rm H}(\hat{\boldsymbol{n}}, v)\sin 2\theta_{\rm H}(\hat{\boldsymbol{n}}, v), \tag{14}$$

where $\theta_{\rm H}$ is the polarization angle perpendicular to the orientation of the local linear structure determined by the Hessian, and $w_{\rm H}$ is formed from the negative eigenvalues as described in Section 3.2. These maps are then summed over velocity as in Equations (11) and (12) to produce $Q_{\rm H}(\hat{\boldsymbol{n}})$ and $U_{\rm H}(\hat{\boldsymbol{n}})$.

Although work conducted across extensive portions of the high-Galactic latitude sky indicates that there could be a minor uniform misalignment between the filaments and the orientation of the magnetic field as measured by Planck, the angle of misalignment amounts to approximately $\sim 2^\circ$–5° only (Huffenberger et al. 2020; Clark et al. 2021; Cukierman et al. 2023). Rotating the H I-based polarization template angles by this amount to emulate this misalignment effect leads to only a slight enhancement in the correlation at the level of $\sim$0.1%–0.5% (Cukierman et al. 2023), and we do not apply this rotation here.

4. Improvements in H I-based Dust Polarization Prediction

In this section, we employ the Hessian algorithm on HI4PI and GALFA-H I data to construct H I-based polarization templates. Working within the Hessian-based framework, we examine how to construct templates that correlate most strongly with Planck polarized dust emission maps. We later contrast these templates with alternative maps based on the Spherical RHT.

4.1. Velocity Selection

Since we expect the correlation between H I and dust to vanish for high-velocity clouds (Wakker & Boulanger 1986; Planck Collaboration et al. 2011; Lenz et al. 2017), we restrict the velocity range over which we integrate the H I-based polarization template in Figure 1. More generally, any contribution to the H I-based polarization template from noise, data artifacts, or H I emission that is not correlated with dust structure will tend to decrease the measured correlation between the template and the polarized dust emission. To restrict the velocity range, we calculate the correlation ratio defined as

$$r_{\ell}^{\rm data\times H\,I} = \frac{D_{\ell}^{\rm fm\times H\,I}}{\sqrt{D_{\ell}^{\rm hm1\times hm2} \times D_{\ell}^{\rm H\,I\times H\,I}}}, \tag{15}$$

where $D_{\ell}^{m_1\times m_2}$ is the cross-spectrum bandpower between two maps, m_1 and m_2, in the multipole bin ℓ. All power spectra in

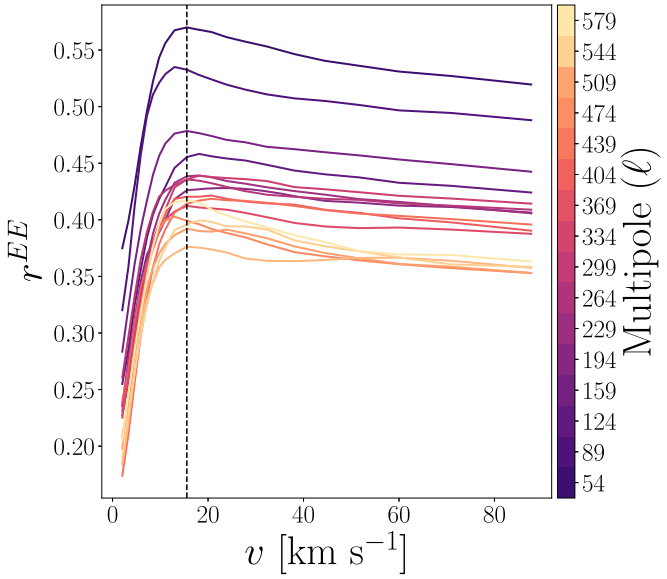

Figure 1. The *EE* correlation ratio on the Planck 70% sky fraction Galactic plane mask of the Planck Commander dust maps with H I-based polarization templates produced by the Hessian algorithm applied to HI4PI data. The leftmost point is for the H I-based polarization template at 2.03 km s^{-1}, and each successive point on each curve corresponds to the addition of information from the two adjacent velocity channels in the positive and negative directions. The labels on the horizontal axis correspond to the velocity centers of the positive velocity channels being added. The different curves correspond to different multipole bins shown in the color bar. The vertical dashed line corresponds to the integrated H I-based polarization template over the velocity range -13 km s^{-1} $< v_{\rm lsr} <$ 16 km s^{-1}, after which the correlation saturates and starts decreasing over most of the multipole bins considered as information from more velocity channels is added.

this paper are computed with the pspy[6] code (Louis et al. 2020). We use the Planck Commander dust maps as the *data*, where the full-mission maps (*fm*) are used for the cross spectra with the H I-based polarization template and the half-mission splits (*hm1* and *hm2*) are used in the denominator. The *H I* in this equation refers to the H I-based polarization template, which in this case is constructed using the Hessian algorithm on the HI4PI data set.

The linear polarization field described by the Stokes *Q* and *U* maps can be decomposed into *E*-mode and *B*-mode components (Seljak & Zaldarriaga 1997; Zaldarriaga 2001). In Equation (15), *data*×*H I* can be the correlation of any combination of the *E*-mode, *B*-mode, or intensity components of the Planck Commander dust maps and the H I-based polarization templates. For example, in Figure 1, we calculate Equation (15) for their *E*-mode components. We do not show the *BB* correlation ratio because it exhibits similar behavior. We use the Planck 70% sky fraction Galactic plane mask for the correlation ratio calculations in this figure. We use the same multipole binning used in BICEP/Keck Collaboration et al. (2023) for a direct comparison of results and because we did not find that multipoles higher than 600 provide additional insights. We start with the H I-based polarization template of the individual velocity channel at $v_{\rm lsr} = 2.03$ km s^{-1}. We pick this velocity channel because it has the highest H I intensity integrated over the unmasked sky. We plot the correlation ratio as a function of velocity integration range and spatial scale in Figure 1. The *x*-axis on this figure is cumulative, i.e., moving toward higher velocities on these plots corresponds to symmetrically integrating outwards in the positive and negative directions from the starting velocity channel, adding one H I-based polarization template from each direction to the previous H I-based polarization template.

The correlation ratio in all multipole bins saturates and even starts decreasing as information from more channel maps is added after a certain velocity. We conclude from this analysis that the H I-based polarization template is most strongly correlated with the polarized dust emission in the range -13 km s^{-1} $< v_{\rm lsr} <$ 16 km s^{-1} over most of the multipole bins considered. We find the same range for *B* modes as well. We use this cut for the rest of the analysis in this paper. Note that the correlation is already at the ∼20%–40% level for the H I-based polarization template of the individual velocity channel at $v_{\rm lsr} = 2.03$ km s^{-1}.

Cukierman et al. (2023) restrict the velocity range to -15 km s^{-1} $< v_{\rm lsr} <$ 4 km s^{-1}. With our velocity selection, we achieve an additional ∼5% increase in the *EE* and *BB* correlation ratios with the Planck Commander dust maps relative to Cukierman et al. (2023). Panopoulou & Lenz (2020) propose the range -12 km s^{-1} $< v_{\rm lsr} <$ 10 km s^{-1} for low-velocity clouds (LVCs). These are the 1st and 99th percentiles of the velocity distribution of clouds with H I column density $N_{\rm H\,I} > 2.5 \times 10^{20}$ cm^{-2} located in the Northern and Southern Galactic Polar regions. The velocity selection we make is close to this range. A benefit of restricting our analysis to this velocity range is that our template is less likely to include contributions from gas at very different distances, which decreases the likelihood of mixing different physical scales.

Using the RHT algorithm for determining the polarization angle, the H I intensity maps as the weighting (see Section 4), and the Spearman rank correlation coefficient and mean angle alignment as the correlation metrics, Clark & Hensley (2019) did not see the decrease in the correlation after a certain velocity that we see in Figure 1. The correlation asymptotes instead. There is also evidence that the intermediate velocity cloud (IVC) gas is organized into filaments that are aligned with their local magnetic fields (Panopoulou et al. 2019; Pelgrims et al. 2021). The difference could be caused by the Hessian algorithm being more sensitive than the RHT to artifacts in low-signal velocity channels. We explore this in Section 4.3.

4.2. Dust Map and Mask Comparisons

We examine how the choice of dust emission maps and sky masks affects the correlation with the H I-based polarization template constructed using the Hessian algorithm on the aforementioned velocity selection in HI4PI data. We compare the *E*- and *B*-mode correlation ratios with the H I-based polarization template on the 70% sky fraction mask between the Planck Commander dust maps at 353 GHz and the Planck frequency maps at 353 GHz in Figure 2. We note that the difference is negligible in *B* modes and at low multipoles in *E* modes. The Commander dust maps correlate more strongly than the Planck frequency maps at higher multipoles in *E* modes. This is due to the CMB *E* modes, which contribute ∼10% of the *E*-mode power to the 353 GHz frequency maps at $\ell > 300$. We therefore use the Commander dust maps for the rest of the analysis in this paper.

We test how the correlation ratio between the Planck Commander dust maps and the H I-based polarization

[6] https://github.com/simonsobs/pspy

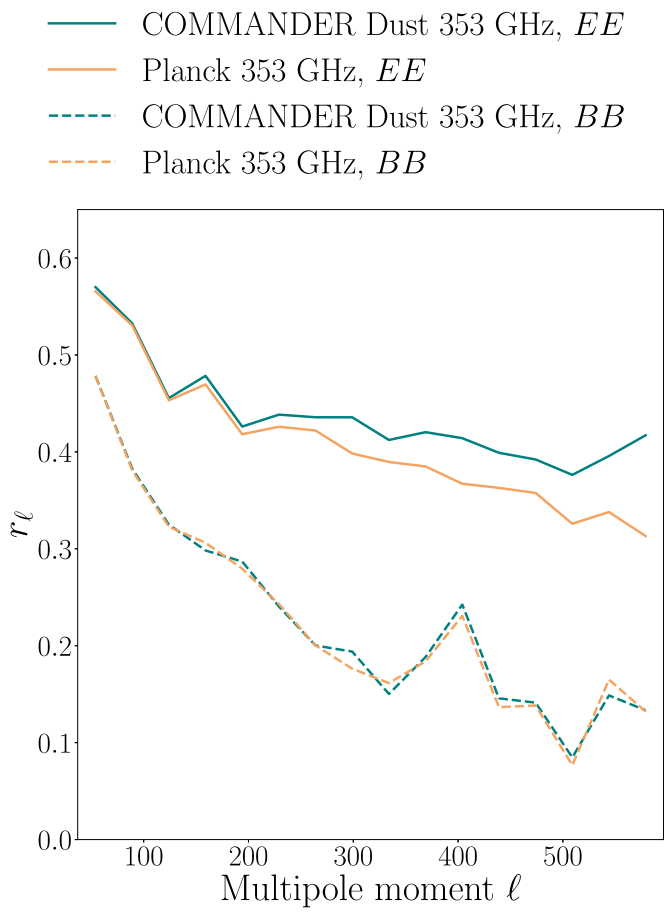

Figure 2. Comparison of the *EE* (solid) and *BB* (dashed) correlation ratios on the Planck 70% sky fraction Galactic plane mask of the Planck `Commander` dust maps (teal) and the Planck frequency maps (sandy brown) at 353 GHz with the H I-based polarization template constructed from applying the Hessian algorithm to HI4PI data at each velocity channel and integrating the resulting maps over the velocity range $-13\ \mathrm{km\ s^{-1}} < v_{\mathrm{lsr}} < 16\ \mathrm{km\ s^{-1}}$.

template changes at different Galactic latitudes by utilizing the Planck sky fraction masks mentioned in Section 2. We invert the 80% sky fraction Galactic plane mask by switching ones to zeros, and vice versa, and call this the low-Galactic-latitude 20% mask. We analyze the results for the high-Galactic latitude 20% sky fraction mask, the low-Galactic-latitude 20% mask, and the differences between the 20% and 40%, 40% and 60%, and 60% and 80% sky fraction Galactic plane masks. These five masks are shown in Figure 3, along with the *EE* and *BB* correlation ratios calculated over these masks. Although a significant portion of the dust column stops being traced by H I at lower Galactic latitudes because it is associated with molecular gas there (Lenz et al. 2017), we find a ∼20% correlation with the low-Galactic-latitude 20% mask up to multipoles of $\ell \sim 400$. Since the velocity selection was optimized for the 70% sky fraction Galactic plane mask, we test whether the reported correlations calculated with the low-Galactic-latitude 20% mask increase when the H I-based polarization templates are integrated over a wider velocity range. We find that the correlation steadily increases over the entire multipole range considered with each template added out to $\pm 90\ \mathrm{km\ s^{-1}}$, reaching ∼68% at $\ell \sim 50$ in *EE*. This increase is expected because our initial velocity selection includes less than 47% of the total Galactic H I column density in this mask.

4.3. Effects of Resolution and Data Artifacts

In the previous subsections, we have only applied the Hessian to HI4PI data, which has an angular resolution of 16.′2, using $N_{\mathrm{side}} = 1024$. In this subsection, we apply the Hessian algorithm to GALFA-H I data, which has a much finer angular resolution of 4′, using $N_{\mathrm{side}} = 2048$. The velocity binning between the HI4PI and GALFA-H I data sets is different, so we use the closest velocity range we can define for the GALFA-H I data set to the velocity selection we found using the HI4PI data set, which is $-15\ \mathrm{km\ s^{-1}} < v_{\mathrm{lsr}} < 18\ \mathrm{km\ s^{-1}}$. However, as shown in Figure 1, most of the correlation comes from the H I emission near the local standard of rest, and we find the difference in dust correlation between the velocity ranges $-15\ \mathrm{km\ s^{-1}} < v_{\mathrm{lsr}} < 18\ \mathrm{km\ s^{-1}}$ and $-11\ \mathrm{km\ s^{-1}} < v_{\mathrm{lsr}} < 15\ \mathrm{km\ s^{-1}}$ to be negligible.

We find that the Hessian algorithm highlights any structure with significant local curvature, which includes scan-pattern artifacts and other emission that is irrelevant to the physical gas filament distribution. To demonstrate this, we apply the Hessian method to a high-velocity channel from GALFA-H I centered on $v_{\mathrm{lsr}} = 400.1\ \mathrm{km\ s^{-1}}$, which has relatively little emission above the noise level in the region analyzed. We compare the polarized intensity maps of an example patch of sky of H I-based polarization templates constructed using the Hessian and RHT algorithms applied to this channel in Figure 4. Polarized intensity is defined as

$$P = \sqrt{Q^2 + U^2}, \tag{16}$$

where Q and U are the Stokes parameter maps of the H I-based polarization template at $v_{\mathrm{lsr}} = 400.1\ \mathrm{km\ s^{-1}}$ in this case. The RHT algorithm is discussed in 3.1. The input intensity map in this figure clearly shows the scan-pattern artifacts. The same artifacts are also obvious in the polarized intensity maps of the Hessian-based template and the first RHT-based template. However, they become much less obvious in the second RHT-based template with different parameters. This shows a limitation of the Hessian method, which the RHT algorithm can be tuned to avoid. This supports the hypothesis made in Section 4.1 concerning the decrease in the correlation with polarized dust emission when incorporating higher velocity channels beyond a specific threshold, which is observed only when using the Hessian method (Figure 1) but not when using the RHT algorithm (Clark & Hensley 2019).

To mitigate this limitation, we experimented with various sensitivity-based weighting schemes for downweighting the low-intensity map pixels in each H I channel. We apply the Hessian algorithm to these new maps and find this weighting to have a negligible effect on the correlation ratio with polarized dust emission. This is true when using both GALFA-H I and HI4PI data for the H I intensity. This implies that the low-intensity H I pixels do not strongly affect the template, i.e., it is not necessarily the low-intensity pixels that contain emission that is uninformative about filament orientations. Rather, this uninformative emission is likely scan-pattern artifacts and other data systematics.

To modify the scale of structure that the Hessian algorithm is most sensitive to, we apply a Gaussian smoothing kernel to each of the GALFA-H I intensity maps before applying the Hessian algorithm. Figure 5 shows the effect of smoothing before applying the Hessian. The maps shown are projections

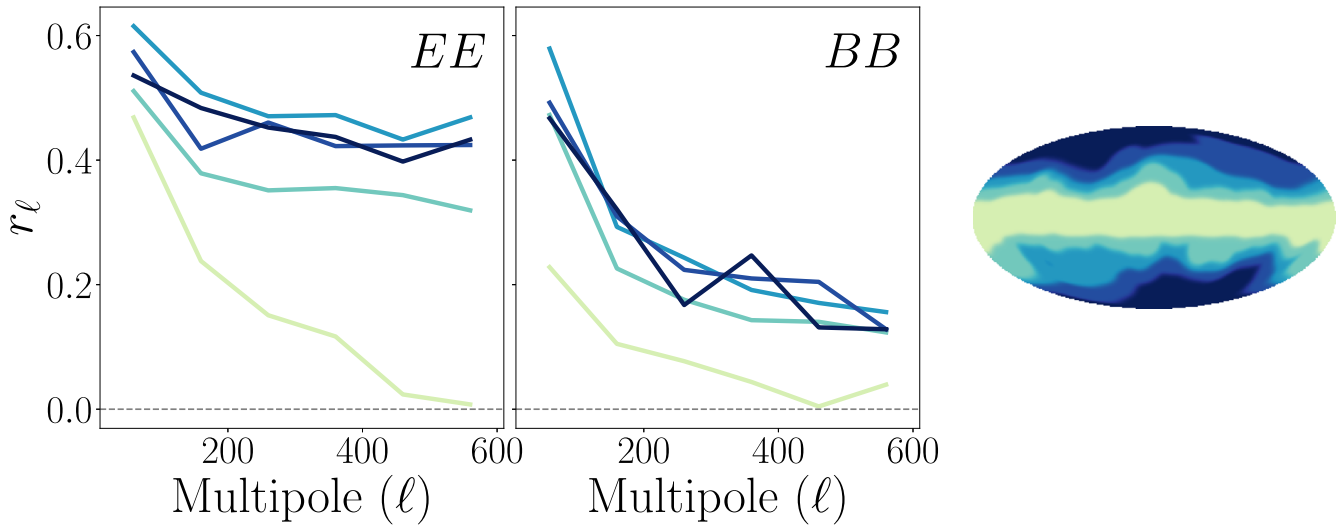

Figure 3. The *EE* (left) and *BB* (middle) correlation ratios of the Planck `Commander` dust maps with the H I-based polarization template constructed using the Hessian algorithm on the HI4PI intensity maps over the different non-overlapping masks shown on the right. The masks are the Planck 20% sky fraction Galactic plane mask (darkest), the inverted Planck 80% sky fraction Galactic plane mask (lightest), and the differences between the Planck 20%, 40%, 60%, and 80% sky fraction Galactic plane masks (other shades of blue) shown in a Mollweide projection in Galactic coordinates centered on the Galactic center.

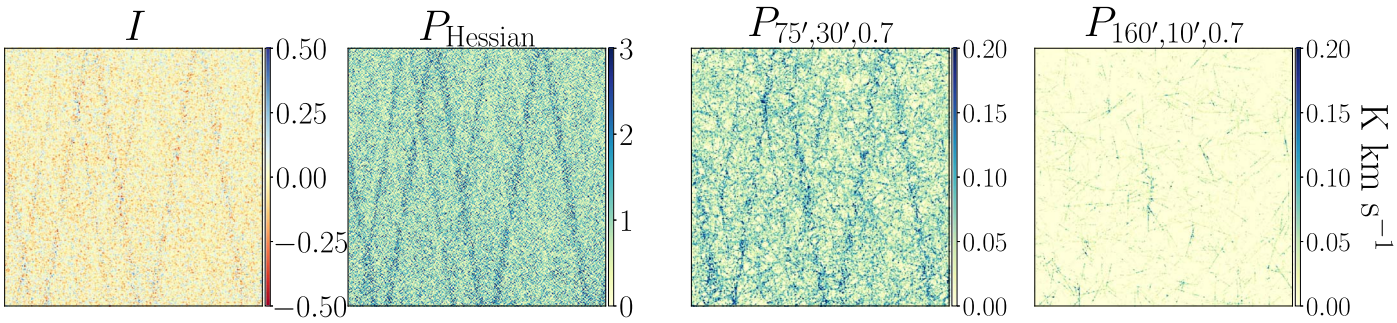

Figure 4. Maps of a 15° × 15° patch of sky centered on R.A. = 7.°5, decl. = 28.°1 and $v_{\rm lsr} = 400.1$ km s^{-1} of the input intensity channel from GALFA-H I with width 0.74 km s^{-1} (left) and polarized intensity of H I-based polarization templates constructed using the Hessian (middle left) and RHT (middle right and right) algorithms applied to this channel. The three parameters listed in the titles of the polarized intensity maps produced with the RHT algorithm are $D_{\rm W}$, $\theta_{\rm FWHM}$, and Z, respectively, explained in Section 3.1.

of the polarized intensity over the velocity selection described in Section 4.1 of an example patch of sky. The first map on the left corresponds to the Hessian algorithm run on the GALFA-H I intensity maps at their native resolution of 4′. Note that it is difficult to see the filamentary structure because the Hessian algorithm is sensitive to other local variations, such as noise and scan-pattern artifacts. Each of the maps to the right of the first one corresponds to the Hessian algorithm applied to the GALFA-H I intensity maps smoothed with a Gaussian kernel to the labeled FWHM resolution. Increasing the FWHM emphasizes real filamentary structure but also makes the filaments wider. We include maps for FWHM = 16′ and 36′, which are the native resolutions of HI4PI and the Leiden/Argentine/Bonn (LAB) surveys (Kalberla et al. 2005), respectively. We include the projection of the polarized intensity of an example patch of the sky when the Hessian algorithm is applied to HI4PI data at their native resolution of 16′ on the right of the figure for comparison with the map titled FWHM = 16′. The velocity binning and the velocity range over which the templates of the two data sets are integrated are not identical, so we do not expect their resulting polarized intensity maps to be identical. When smoothed to the HI4PI beam, the GALFA-H I maps are modestly more sensitive.

Smoothing the H I data before constructing the H I-based polarization templates deemphasizes small-scale noise at the cost of sensitivity to real small-scale H I structure that may correlate well with the measured polarized dust emission. We explore this trade-off in GALFA-H I data by calculating the *EE*, *BB*, and *TE* correlation ratios of the different maps in Figure 5 with the Planck `Commander` dust maps and plot the results in Figure 6. For the *TE* case, we correlate the Planck dust total intensity with the templates' *E* modes.

The trend is not consistent between the three panels. The *TE* correlation simply increases as the GALFA-H I data are smoothed, with an expected dip at the smoothing scale, which is only within the multipole range considered for the FWHM = 36′ case. However, the *EE* and *BB* correlations are maximized when the H I data are smoothed to intermediate resolutions. While an increase in the *EE* and *BB* correlation ratios is what we should aim for, an increase in the *TE* correlation ratio is not necessarily better since we expect the real *TE* correlation ratio to be ∼0.36 (Planck Collaboration et al. 2020c). Therefore, a near-ideal *E*-mode template should correlate with the Planck dust total intensity at about that level. However, in all cases, we achieve a significant improvement in the correlation with polarized dust emission by smoothing the map before applying the Hessian algorithm. The H I-based

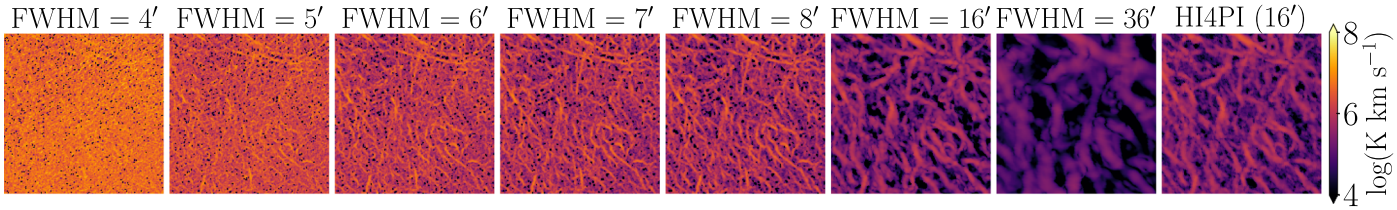

Figure 5. Polarized intensity map projections of a 400′ × 400′ patch of sky, centered at (l, b) = (15°, 50°), of H I-based polarization templates constructed using the Hessian algorithm applied to GALFA-H I intensity maps smoothed to different resolutions. The intensity map corresponding to the leftmost polarized intensity map is not smoothed, i.e., it has the native resolution of GALFA-H I. The intensity maps corresponding to the polarized intensity maps to the right of the first map are smoothed with Gaussian kernels to the resolution stated in their titles. The last map on the right corresponds to the Hessian algorithm applied to HI4PI data at its native resolution, though it is integrated over a slightly different velocity range as mentioned in Section 4.3.

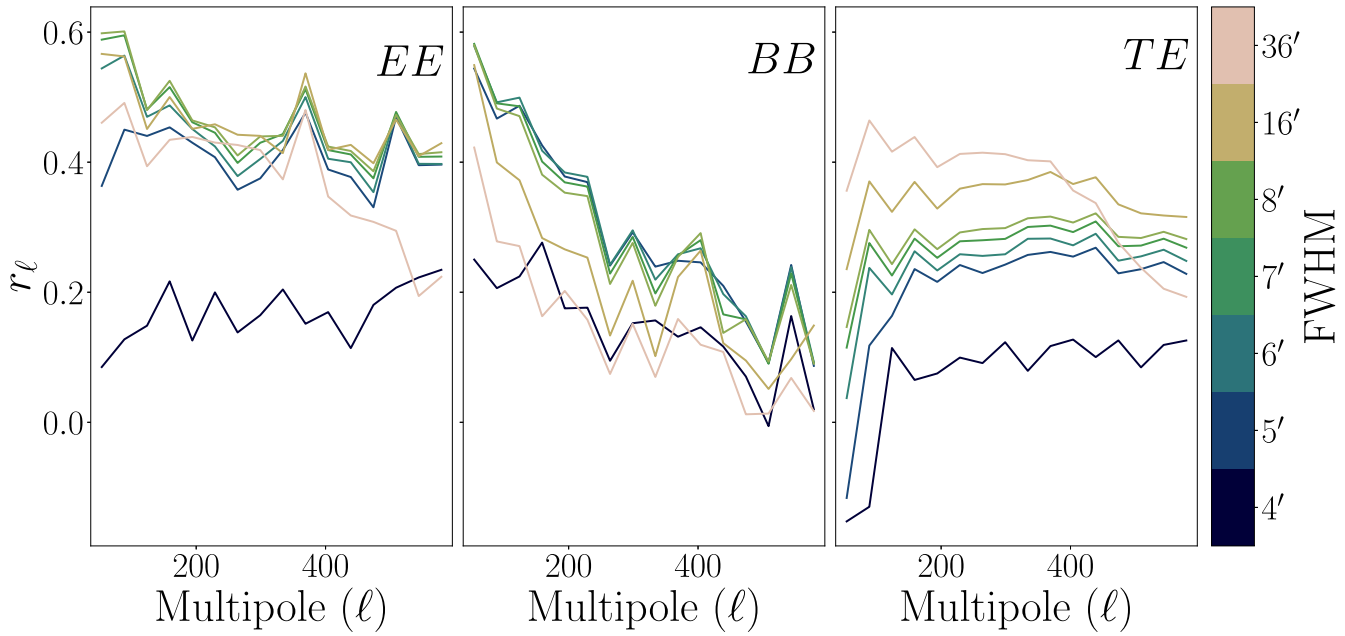

Figure 6. The *EE* (left), *BB* (middle), and *TE* (right) correlation ratios between the maps in Figure 5 and the Planck `Commander` dust maps at 353 GHz. The *TE* correlation ratio measures the correlation between the Planck total intensity and the templates' *E* modes. Correlations are computed on a combination of the GALFA-H I and Planck 70% sky fraction masks.

polarization template based on HI4PI data at their native 16′ resolution is similarly correlated with the dust polarization to the template based on the GALFA-H I data smoothed to 16′. The map smoothed to 36′ decreases both the *EE* and *BB* correlations with the Planck `Commander` dust maps. This shows the utility of the higher-resolution H I intensity data from the GALFA-H I and HI4PI surveys in modeling polarized dust emission over the lower-resolution LAB survey.

We compare the H I-based polarization templates based on GALFA-H I data smoothed to FWHM = 7′ and on HI4PI data by plotting their *EE* and *BB* correlation ratios with the Planck `Commander` dust maps at 353 GHz in Figure 7. We use a ∼23% sky fraction mask by combining the GALFA-H I mask with the Planck 70% sky fraction mask. The H I-based polarization template constructed from the GALFA-H I data set is more strongly correlated in *B* modes with the polarized dust emission than that constructed using the HI4PI data set. The improvement is at the ∼10% level at multipoles $\ell < 350$. This implies that higher-resolution H I data are useful for better modeling the polarized dust foreground in *B* modes. If we smooth the GALFA-H I data set to a resolution of FWHM = 16′ (the resolution of HI4PI) instead of 7′, the *BB* improvement becomes negligible.

The *EE* and *BB* correlation ratios between the H I-based polarization template constructed from HI4PI data and the Planck `Commander` dust maps at 353 GHz do not increase after smoothing the HI4PI data set. For the rest of the analysis in this paper, we use the HI4PI data set at its native resolution.

5. Spherical Rolling Hough Transform

As discussed in the previous section, the Hessian algorithm is sensitive to the local curvature in images and thus is most sensitive to structure at the image resolution. To explore different filament morphologies, however, we need an algorithm with free parameters that help set the scale and shape of the identified filaments. One such algorithm is the RHT (Clark et al. 2014, 2020) described in Section 3.1.

The code for the RHT algorithm is publicly available and has been applied to a variety of astronomical images, including molecular clouds (Malinen et al. 2016; Panopoulou et al. 2016), magnetohydrodynamic simulations (Inoue & Inutsuka 2016), depolarization canals (Jelić et al. 2018), the solar corona (Boe et al. 2020), and supernova remnants (Raymond et al. 2020). The algorithm has been adapted to work on resolved stars for stellar stream detection (Pearson et al. 2022) and extended to add the ability to identify filaments with user-specified widths (Carrière et al. 2022).

The RHT algorithm currently runs on flat-sky projections of small patches of the sky. Therefore, to achieve results over the full sky, small patches of the spherical map need to be projected into separate flat-sky images. This is time-consuming and the reprojection step may produce distortion effects. Hence, we implement an alternative algorithm that enables RHT computation directly on the sphere by utilizing spherical harmonic convolutions.

5.1. Spherical Convolutions

In a flat geometry, a convolution between two maps can be computed from the product of their Fourier representations. On the sphere, the convolution can be expressed similarly as a product of their spherical harmonic representations. A major difference, however, is that the spherical harmonic representation is weighted by Wigner matrices (Wandelt & Górski 2001; Prézeau & Reinecke 2010). The convolution of a map with spherical harmonics $a_{\ell m}$ and a convolution kernel defined on the sphere with spherical harmonics $b_{\ell m'}$ for Euler angles (α, β, γ) can be written as

$$c(\alpha, \beta, \gamma) = \sum_{m'=-m'_{\rm max}}^{m'_{\rm max}} \sum_{m=-\ell_{\rm max}}^{\ell_{\rm max}} e^{im'\alpha} e^{im\gamma} C_{m'm}(\beta), \quad (17)$$

where

$$C_{m'm}(\beta) \equiv \sum_{\ell=0}^{\ell_{\rm max}} b^*_{\ell m'} D^{\ell}_{m'm}(\beta) a_{\ell m}, \quad (18)$$

and $D^{\ell}_{m'm}$ are the so-called Wigner matrices. In our case, α would represent the orientation of the convolution kernel, and β and γ represent the latitude and longitude of the sky, respectively. Refer to Prézeau & Reinecke (2010) for more details.

The computation of the Wigner matrices is usually the bottleneck of convolution algorithms. This is a major problem in CMB analyses in the context of beam convolutions (e.g., Challinor et al. 2000). If the convolution kernel is restricted to a small set of m' values, then the algorithm can run faster. An example is a symmetric beam, which is restricted to $m = 0$. Our filamentary kernels are not symmetric, but we can limit the maximum m' value and retain the intended shape as described in Section 5.2. We use `ducc`,[7] a computationally efficient code for performing convolutions with axially asymmetric convolution kernels.

5.2. The Algorithm

We implement the steps described in Section 3.1 directly on the sphere rather than on flat-sky image projections. We call this new implementation the spherical Rolling Hough Transform (Spherical RHT). This implementation replaces Step 3 of the RHT algorithm in Section 3.1 with the spherical harmonic convolutions described in Section 5.1. We show a diagram of the full procedure in Figure 8. This diagram shows how the parameters $\theta_{\rm FWHM}$, $D_{\rm W}$, and Z are used to transform the H I intensity at each velocity channel v and pixel $\hat{n}$ into $R(\hat{n}, \theta, v)$, which is used in Equations (8), (9), and (10) to construct the H I-based Stokes Q and U maps for that velocity channel.

We define a convolution kernel as a line of neighboring nonzero pixels of length $D_{\rm W}$ on a HEALPix grid of a higher resolution than the maps we convolve it with. We then smooth this line of pixels so that the pixelization of the lower-resolution maps captures all of the information in the kernel. This prevents aliasing from small scales that the pixelization of the lower-resolution maps is insensitive to. For instance, when run on HI4PI data at $N_{\rm side} = 1024$, we define the kernel at $N_{\rm side} = 4096$ and smooth it to a FWHM of 3.′4, the width of a pixel at $N_{\rm side} = 1024$.

We find that limiting the $m'_{\rm max}$ of the kernel to 50 retains the intended shape of the kernel visually. Also, the results in this paper are identical when $m'_{\rm max}$ is increased to 100. Limiting the $m'_{\rm max}$ of the convolution kernel increases the computational efficiency of the algorithm.

We convolve this kernel at different orientations with the map as described in Section 5.1. In the standard RHT algorithm, the number of orientations depends on $D_{\rm W}$. For all $D_{\rm W}$ used in this paper, dividing the kernel orientations into 25 bins yields consistent results to dividing them into 300 bins. Therefore, we use 25 orientations for computational efficiency. However, the number of orientations is left as a free parameter in the code in case more orientations are necessary for different applications. The code is made publicly available on GitHub[8] (Halal et al. 2023).

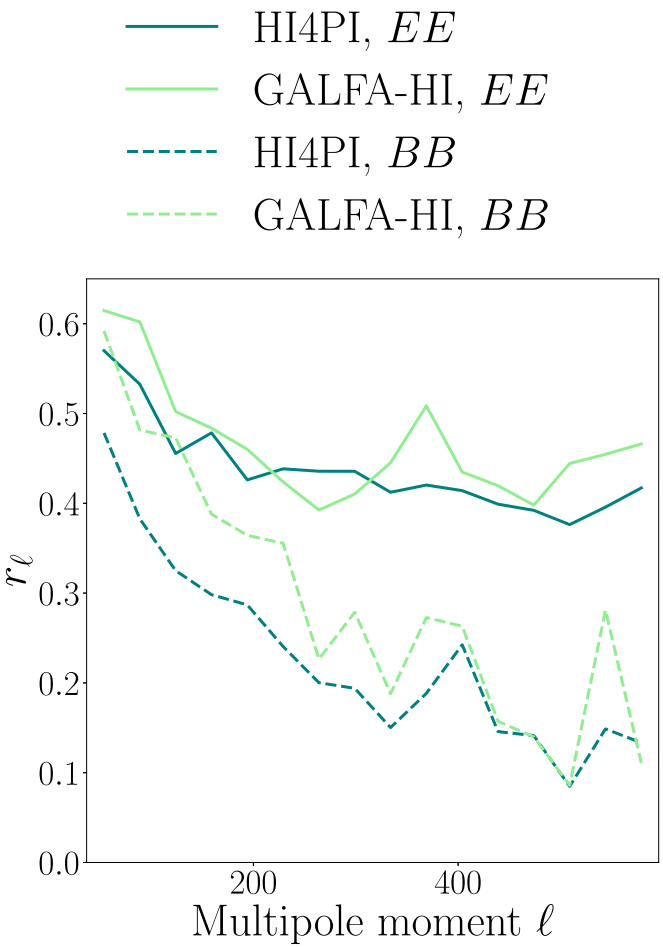

Figure 7. Comparison of the *EE* (solid) and *BB* (dashed) correlation ratios with the Planck `Commander` dust maps at 353 GHz of the H I-based polarization templates using GALFA-H I data smoothed to a FWHM of 7′ (light green) and HI4PI data (teal). The H I-based polarization templates are integrated over a similar velocity range and constructed using the Hessian algorithm. The correlations are calculated on a combination of the GALFA-H I mask with the Planck 70% sky fraction mask. The teal lines are the same as those in Figure 2.

[7] https://gitlab.mpcdf.mpg.de/mtr/ducc

[8] https://github.com/georgehalal/sphericalrht

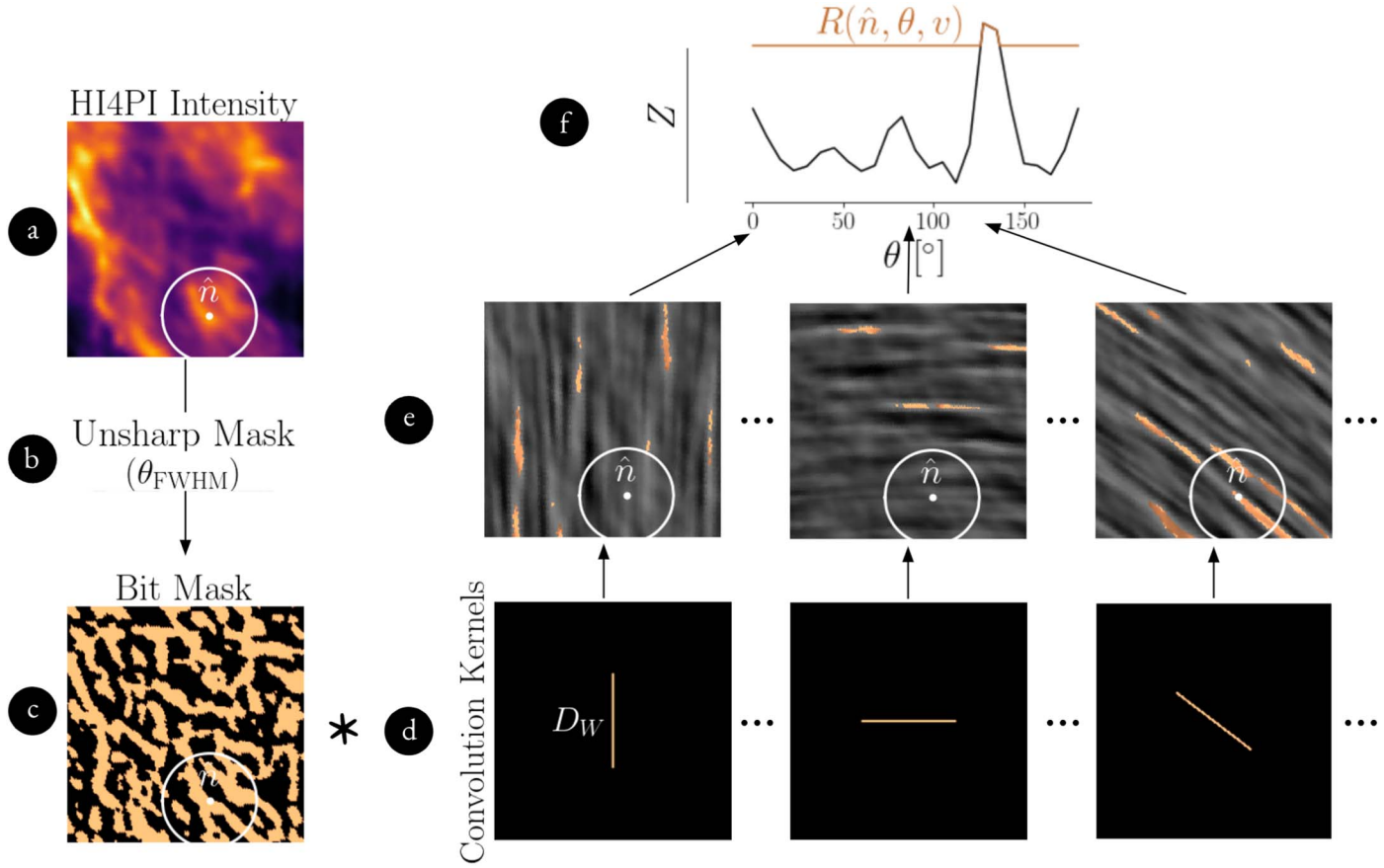

Figure 8. Diagram of the Spherical RHT procedure. (a) A flat-sky projection of a $400' \times 400'$ patch of sky, centered at $(l, b) = (15°, 50°)$ and $v_{\rm lsr} = 2.03$ km s^{-1} for the initial H I intensity channel with width 1.3 km s^{-1} from the HI4PI Survey. The diameter of the white circle drawn around pixel $\hat{n}$ is equal to $D_{\rm W}$, the length of the convolution kernels, three of which are shown to scale (d). We chose $D_{\rm W} = 160'$ in this case. (c) The resulting binary map of the preprocessing steps (b; Steps 1 and 2 in Section 3.1) with $\theta_{\rm FWHM} = 10'$ applied to (a). The convolution kernels (d) are both rotated and convolved with (c) in spherical harmonic space. (e) The results of the convolutions between (c) and (d). (f) The result of the convolutions for pixel $\hat{n}$ over orientations θ. A threshold, $Z = 0.7$ in this case, is applied to the result of the convolutions (Step 4 in Section 3.1), leaving $R(\hat{n}, \theta, v)$; (copper). The colors in (e) and (f) are set to match, i.e., the pixels (e) have a copper-like color scale where the resulting intensities (f) pass Z and a gray color scale otherwise.

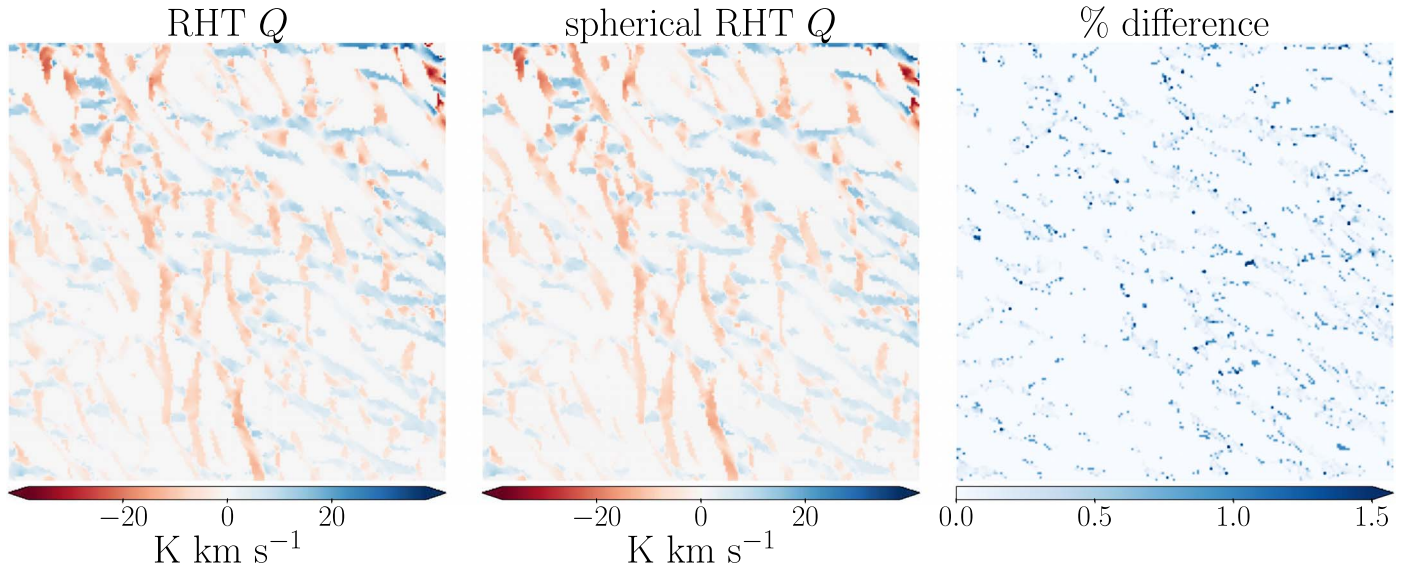

Figure 9. Stokes Q map projections of a $15° \times 15°$ patch of sky, centered at $(l, b) = (15°, 50°)$, of H I-based polarization templates for one velocity slice of the HI4PI Survey centered at $v_{\rm lsr} = 2.03$ km s^{-1} with width 1.3 km s^{-1} constructed using the RHT (left) and the Spherical RHT (middle) algorithms with parameters $D_{\rm W} = 75'$, $\theta_{\rm FWHM} = 30'$, and $Z = 0.7$. The map on the left is used in Clark & Hensley (2019). The map on the right is the percentage difference between the map on the left and the map in the middle.

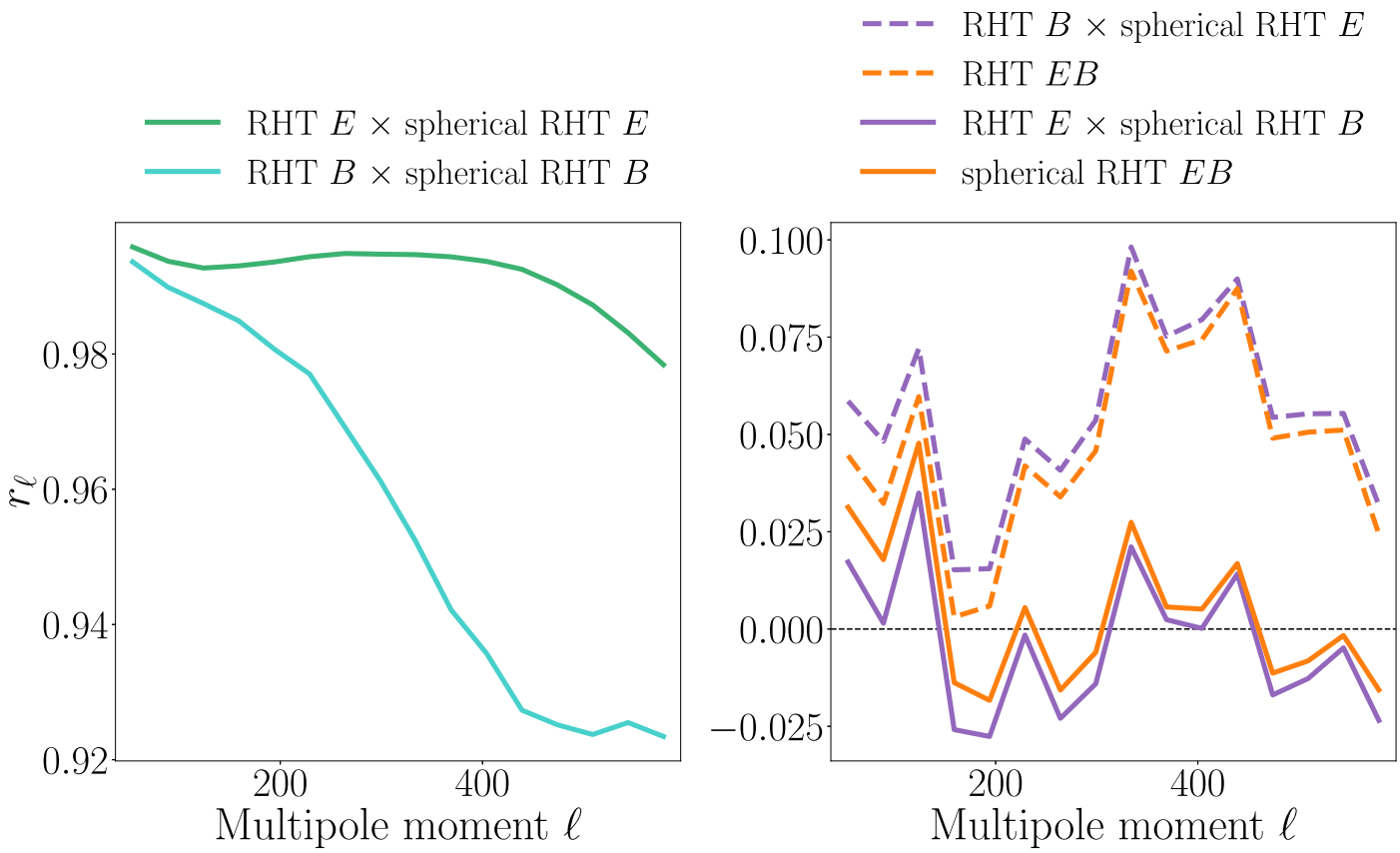

Figure 10. Left: the *EE* (green) and *BB* (blue) correlation ratios between the H I-based polarization template used in Clark & Hensley (2019) and that reproduced using the Spherical RHT algorithm with the same parameters. Right: the *EB* correlation ratios, showing that the likely spurious positive correlation when the *B* modes of the Clark & Hensley (2019) H I-based polarization template are used (dashed) vanish when the curved sky is taken into account and the *B* modes produced with the Spherical RHT algorithm are used (solid). The orange (purple) curves represent correlation ratios where the *E* and *B* modes of the same algorithm (different algorithms) are used. HI4PI data and the Planck 70% sky fraction mask are used in these plots. Note the difference in the y-scales between the left and right panels.

5.3. Comparison with the RHT

We follow the prescription described in Clark & Hensley (2019), replacing the RHT on small flat-sky projections with the Spherical RHT, to construct full-sky H I-based polarization templates and compare the results of the two algorithms.

Once the distribution $R(\hat{\boldsymbol{n}}, \theta, v)$ over orientations θ is obtained for each pixel $\hat{\boldsymbol{n}}$ at each velocity channel v after Step 4 in Section 3.1, Clark & Hensley (2019) construct Stokes $Q_{\rm H\,I}$ and $U_{\rm H\,I}$ maps as in Equations (8), (9), (10), (11), and (12).

We run the Spherical RHT on HI4PI data with the same velocity binning as in Clark & Hensley (2019) and with the same free parameters, $\theta_{\rm FWHM} = 30'$, $D_{\rm W} = 75'$, and $Z = 0.7$, and compare the resulting Stokes Q polarization maps to those of Clark & Hensley (2019) in Figure 9. We show flat-sky projections of an example patch of sky of these maps. We also show the percentage difference between the maps and note that the results are qualitatively the same but not numerically identical, and we do not expect them to be. We note that the difference is mostly concentrated at the edges of the filaments. We do not show the Stokes U results because the conclusions are the same.

To quantitatively test the differences between the two algorithms for constructing H I-based polarization templates, we plot the correlation ratio of all different combinations of the *E* and *B* modes of the two algorithms in Figure 10 using the Planck 70% sky fraction mask. The correlations between the Clark & Hensley (2019) and the Spherical RHT templates are higher than 98% in *E* modes and higher than 92% in *B* modes across all multipoles considered. Since both algorithms assume no misalignment between the filament orientations and the local

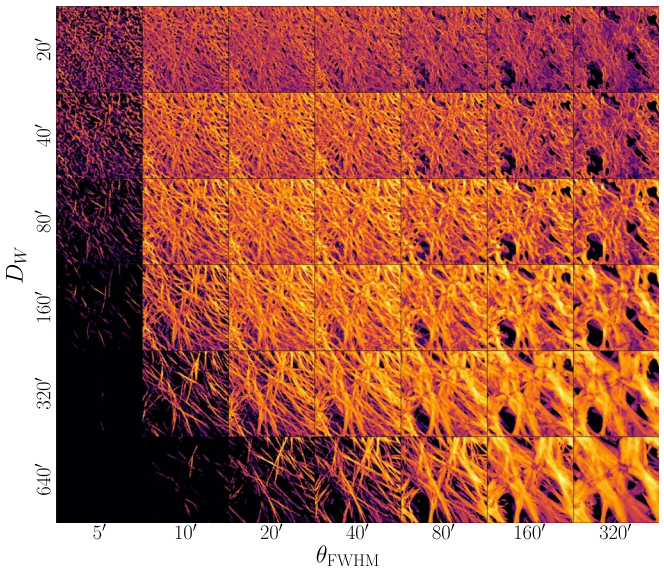

Figure 11. Polarized intensity map projections of a 16.°7 × 16.°7 patch of sky, centered at $(l, b) = (15°, 50°)$, of H I-based polarization templates constructed using the Spherical RHT algorithm with different parameters applied to HI4PI intensity maps. The parameter Z is fixed to 0.7 and the Spherical RHT is run on a grid of exponentially increasing parameters between 5′ and 320′ for $\theta_{\rm FWHM}$ (to the right) and 20′ and 640′ for $D_{\rm W}$ (to the bottom).

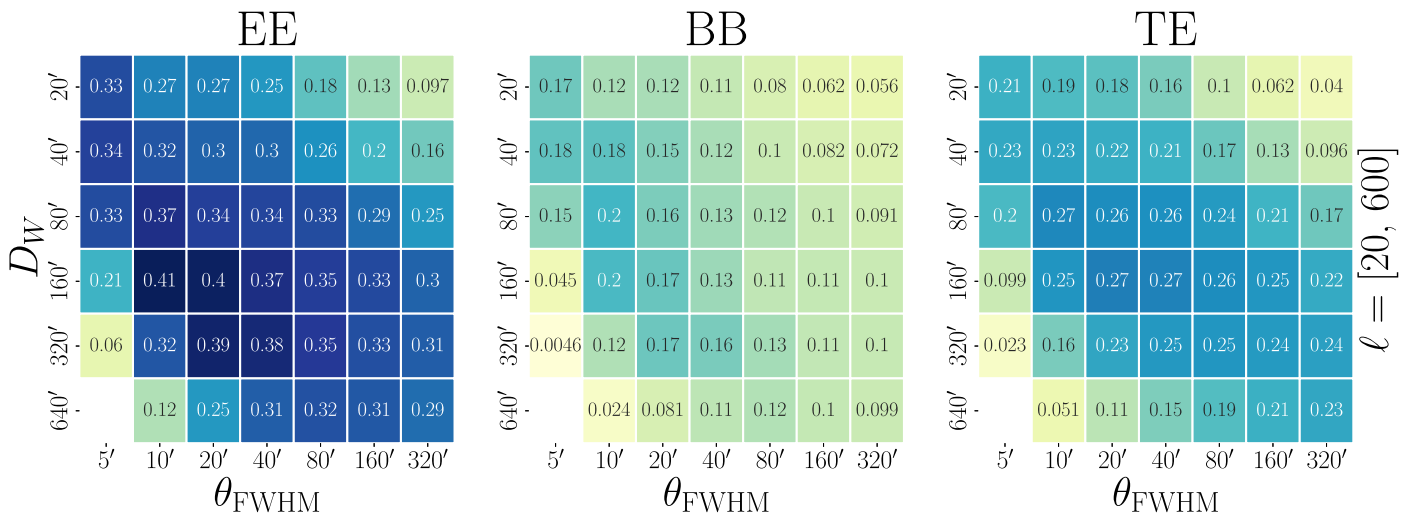

Figure 12. The *EE* (left), *BB* (middle), and *TE* (right) correlation ratios between the maps in Figure 11 and the Planck `Commander` dust maps over a broadband multipole bin between $\ell = 20$ and $\ell = 600$. The Planck total intensity is correlated with the *E* modes of the Spherical RHT–based templates for the *TE* case.

magnetic fields as described in Section 4, we expect the *EB* correlation to be zero unless the morphology of the filaments across the sky has a preferred chirality as described in Section 6.1. The *EB* correlations are negligible in this figure when the *B* modes are predicted by the Spherical RHT algorithm, i.e., when the curved sky is taken into account. However, the *EB* correlations are at the ∼5% level across the multipole range when the *B* modes are predicted by the Clark & Hensley (2019) maps. These results are not latitude dependent. Note that this is not a bug in the RHT code itself. Rather, it is an artifact of projecting each window of the map onto a flat-sky image. While it does not affect any of the results presented in Clark & Hensley (2019), it is preferable for our morphology investigation that the Spherical RHT does not have this property.

6. Filament Morphologies

6.1. Morphological Parameter Space Exploration

The Spherical RHT enables efficient exploration of the $D_{\rm W}$, $\theta_{\rm FWHM}$, and *Z* parameter space that governs how the geometry of the filamentary H I structure is mapped into an H I-based polarization template. We use this to investigate what H I filament morphologies are most predictive of the measured polarized dust emission. This is a continuation of the parameter space exploration performed in BICEP/Keck Collaboration et al. (2023). That work used the RHT on a small patch that covered ∼1% of the sky and assessed the cross-correlation between the H I-based polarization template and multifrequency polarized dust emission data from BICEP/Keck and Planck. Utilizing the Spherical RHT, we extend this analysis to the full sky in this paper.

Using results from the exploration in BICEP/Keck Collaboration et al. (2023), we fix the *Z* parameter to 0.7, such that the algorithm is only sensitive to structures larger than 70% of $D_{\rm W}$. We run the Spherical RHT on a grid of exponentially increasing parameters between 5′ and 320′ for $\theta_{\rm FWHM}$ and 20′ and 640′ for $D_{\rm W}$. We show the polarized intensity maps corresponding to these parameters in Figure 11. We calculate the *EE*, *BB*, and *TE* correlation ratios between these maps and the Planck `Commander` dust maps over a broadband multipole bin between $\ell = 20$ and $\ell = 600$ in Figure 12. For the *TE* case, we compute the correlation between the Planck 353 GHz total intensity and the template *E* modes.

For the lowest $\theta_{\rm FWHM}$ and highest $D_{\rm W}$ case, the RHT intensity is zero because no linear structures cover at least 70% of $D_{\rm W}$ after the unsharp mask step removes structure on scales greater than 5′. By contrast, for the highest $\theta_{\rm FWHM}$ and lowest D_W case, the template morphology is more sensitive to lower-intensity diffuse H I structure, which tends to be less filamentary. This is reflected in the morphology of the H I-based polarization template in the upper right-hand corner of Figure 11. At fixed $\theta_{\rm FWHM}$, the filaments tend to be longer with increasing $D_{\rm W}$, and at fixed $D_{\rm W}$, the filaments tend to be wider with increasing $\theta_{\rm FWHM}$. We find a clear gradient in the correlation coefficient over the parameter space explored with a preference toward $\theta_{\rm FWHM} \sim 10'$–$20'$, i.e., near the 16′ HI4PI beam scale, and $D_{\rm W} \sim 80'$–$160'$. We repeat this exercise for smaller broadband multipole bins and find that the $\theta_{\rm FWHM} \sim 10'$–$20'$ preferred scale does not change, while the preferred scale for $D_{\rm W}$ increases slightly when considering larger scales and decreases slightly when considering smaller scales.

The fact that the preferred $\theta_{\rm FWHM}$ range is approximately at the beam scale indicates that the thinnest resolved filaments are the most informative about the magnetic field orientation. This means that the H I filaments that are best-correlated with the polarized dust emission are somewhat thinner and longer than the structures that the Clark & Hensley (2019) analysis was most sensitive to at $D_{\rm W} = 75'$ and $\theta_{\rm FWHM} = 30'$. We find that the structures that are more qualitatively filamentary in Figure 11 correlate best in all the metrics in Figure 12. The less-linear morphologies that populate the upper right-hand portion of Figure 11 correlate poorly with the Planck data. This indicates that elongated linear structures are genuinely the geometry that best describes the polarized dust emission field within the morphological parameter space we can explore.

In the isolated filament case, *E* modes are primarily sourced along the length of the filament, while *B* modes are primarily sourced at the edges of the filament (Huffenberger et al. 2020). Therefore, the H I-based polarization templates that maximize the *EE* correlation with polarized dust emission are likely the ones that most closely recover the geometry of the dust filaments that dominate the polarized intensity, i.e., their lengths, widths,

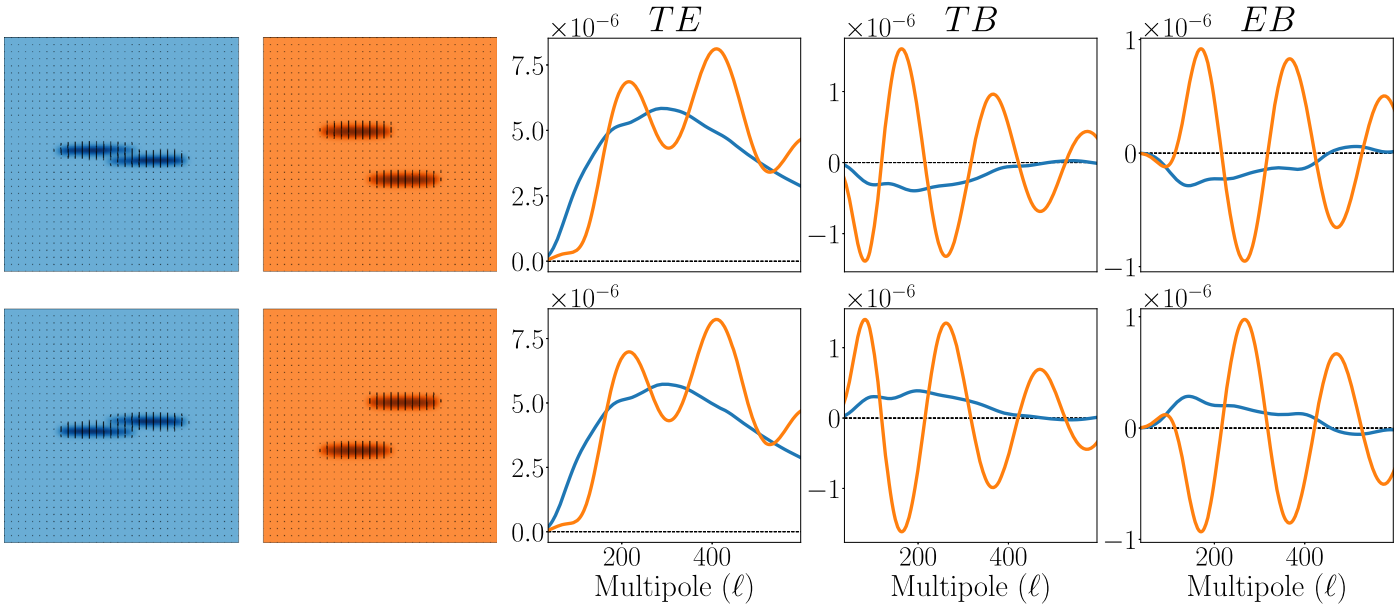

Figure 13. Right panel: the *TE* (left), *TB* (middle), and *EB* (right) cross spectra (D_ℓ) of two synthetic filaments close to each other (blue, left panel) and far from each other (orange, left panel), where the arrangement of the filaments in the top and bottom rows have opposite parities. The headless vectors in the left panels show the polarization angle orientations perpendicular to the lengths of these filaments. The color scale in the left panels represents the polarized intensity.

and orientations. The similarity in the correlation dependence on D_W and θ_{FWHM} between the *EE* and *TE* panels of Figure 12 also supports this conclusion. The H I-based polarization templates that maximize the *BB* correlation with polarized dust emission are likely the ones whose filaments are at the correct distances from each other, which affects the constructive and destructive interference of the *B*-mode patterns.

To illustrate the *E*- and *B*-mode patterns produced in the multifilament case, we run the Spherical RHT algorithm with the parameters used in Clark & Hensley (2019; $D_W = 75'$, $\theta_{FWHM} = 30'$, and $Z = 0.7$) on maps of two synthetic filaments, slightly offset from one another in longitude. Figure 13 shows the results when these filaments are positioned at different distances relative to each other in latitude and when they are reflected relative to each other in longitude. The *TE* spectra are positive whether the filaments are close to or far from one another and are unaffected by the parity of the filaments' relative positions. By contrast, the *TB* spectra fluctuate around zero when the filaments are far from one another but are only positive or only negative, depending on parity, when the filaments are close to one another. This shows how *E* modes mainly depend on the individual filament geometries, whereas *B* modes mainly depend on the geometry of the filaments relative to one another.

Figure 13 is also a demonstration of how the Spherical RHT algorithm can be used as a tool to extend our intuition about morphological features that produce parity-violating signatures, i.e., nonzero *TB* and *EB*. We show positive-only *TB* and *EB* signals when the two filaments are positioned close to one another in one handedness and negative-only signals when those filaments are close to one another in the opposite handedness. Characterizing parity-violating signatures in polarized dust emission is interesting for several applications, including confounding cosmic birefringence searches (Minami & Komatsu 2020) and biasing CMB polarization "self-calibration," which assumes that *TB* and *EB* signals are due to systematic errors because they must vanish in the standard cosmological model (Abitbol et al. 2016). Huffenberger et al. (2020) and

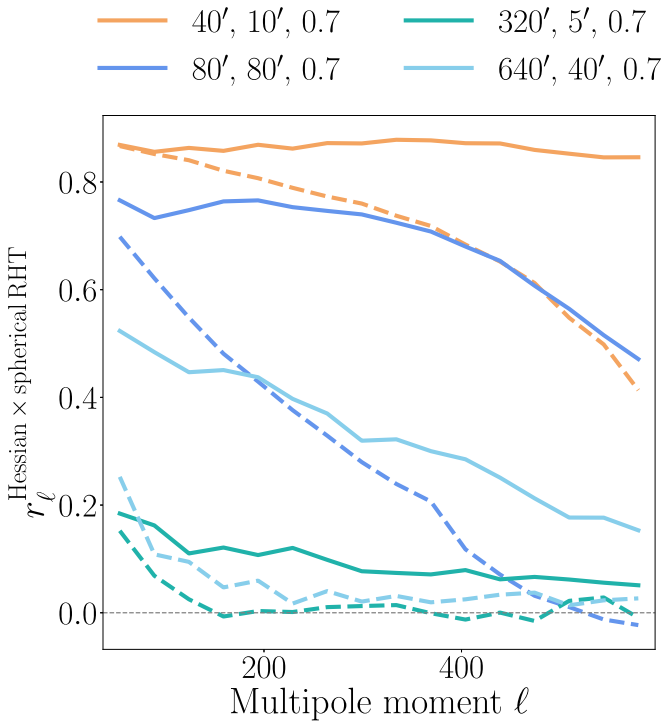

Figure 14. The *EE* (solid) and *BB* (dashed) correlation ratios between the H I-based polarization template constructed using the Hessian algorithm and four H I-based polarization templates constructed using the Spherical RHT algorithm on HI4PI data. The Planck 70% sky fraction mask was used for the spectra used for calculating these correlation ratios. The parameters listed in the legend are the D_W, θ_{FWHM}, and *Z*, respectively, defined in Section 3.1. The first set of parameters (sandy brown) is the one that correlates the best, and the other three are randomly selected.

Clark et al. (2021) have shown that a misalignment between dust filaments and the local magnetic field orientations can produce parity-violating signatures. The H I-based polarization templates assume perfect alignment between the filament morphologies and the magnetic field orientations. However, even without local

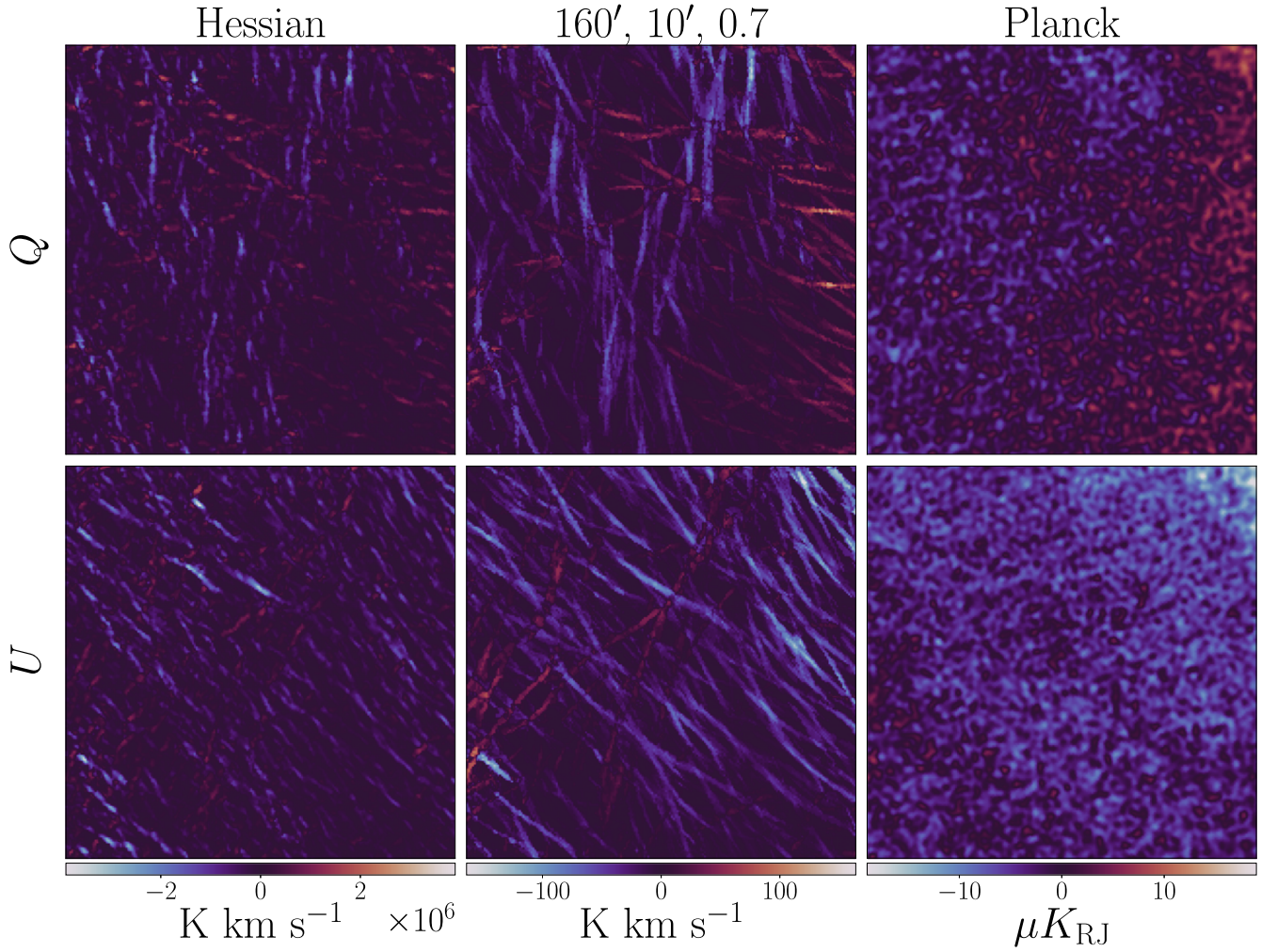

Figure 15. Stokes Q (top) and U (bottom) map projections of a 16.°7 × 16.°7 patch of sky, centered at $(l, b) = (15°, 50°)$, of the H I-based polarization templates constructed using the Hessian method (left) and Spherical RHT algorithm with parameters $D_W = 160'$, $\theta_{FWHM} = 10'$, and $Z = 0.7$ (middle) applied to HI4PI intensity maps, and the full-mission Planck `Commander` dust map (right).

misalignment, chirality in the distribution of filaments or in the non-filamentary polarizing structures could produce these signatures. These may be especially significant on small patches of the sky, whereas the signal may average down if large sky areas show no preferred "handedness" of the dust intensity distribution.

6.2. Spherical RHT- and Hessian-based Template Comparison

We compare the H I-based polarization templates produced using the Spherical RHT algorithm to those produced using the Hessian algorithm to understand the factors that affect the correlation of each with the measured polarized dust emission. We start by cross correlating the Hessian-based template with Spherical RHT–based templates constructed using different parameters. We show the *EE* and *BB* correlation ratios of four of these in Figure 14. All of the spectra use the Planck 70% sky fraction mask. The *BB* correlation ratios are much weaker than the *EE* correlation ratios of the same parameters at small scales —in other words, the Spherical RHT and Hessian templates are more similar to one another in *E* modes than in *B* modes. While we find a set of Spherical RHT parameters that produces a template that correlates at the ∼90% level in *E* modes with the Hessian-based template, none of the parameter sets we test produces a template that correlates higher than ∼60% at $\ell > 500$ in *B* modes.

We plot the Stokes Q and U projections of an example patch of sky for the H I-based polarization templates based on the Hessian method and the Spherical RHT algorithm using the best-correlating parameters we found in Section 6.1 and the full-mission Planck `Commander` dust map in Figure 15. This gives a sense of the different polarization structures predicted by these filamentary templates as compared to the observed total dust field. The Planck maps are noise dominated at small scales. However, the large-scale correspondence is visible in this figure.

We compare the correlation of the H I-based polarization templates from Figure 15 with polarized dust emission. For a broadband multipole bin between $\ell = 20$ and $\ell = 140$ and centered at $\ell = 80$, a range relevant to primordial *B*-mode detection, we find that the *EE* (*BB*) correlation ratios are 0.5 and 0.6 (0.42 and 0.48) for the templates constructed using the Hessian and Spherical RHT algorithms, respectively. We plot the *EE*, *BB*, and *TE* correlation ratios with the Planck `Commander` dust maps as well as the *EE*-to-*BB* autospectra ratio in Figure 16. All of the plots in Figure 16 use the Planck 70% sky fraction mask and HI4PI data. However, the results are qualitatively similar for different sky fraction masks.

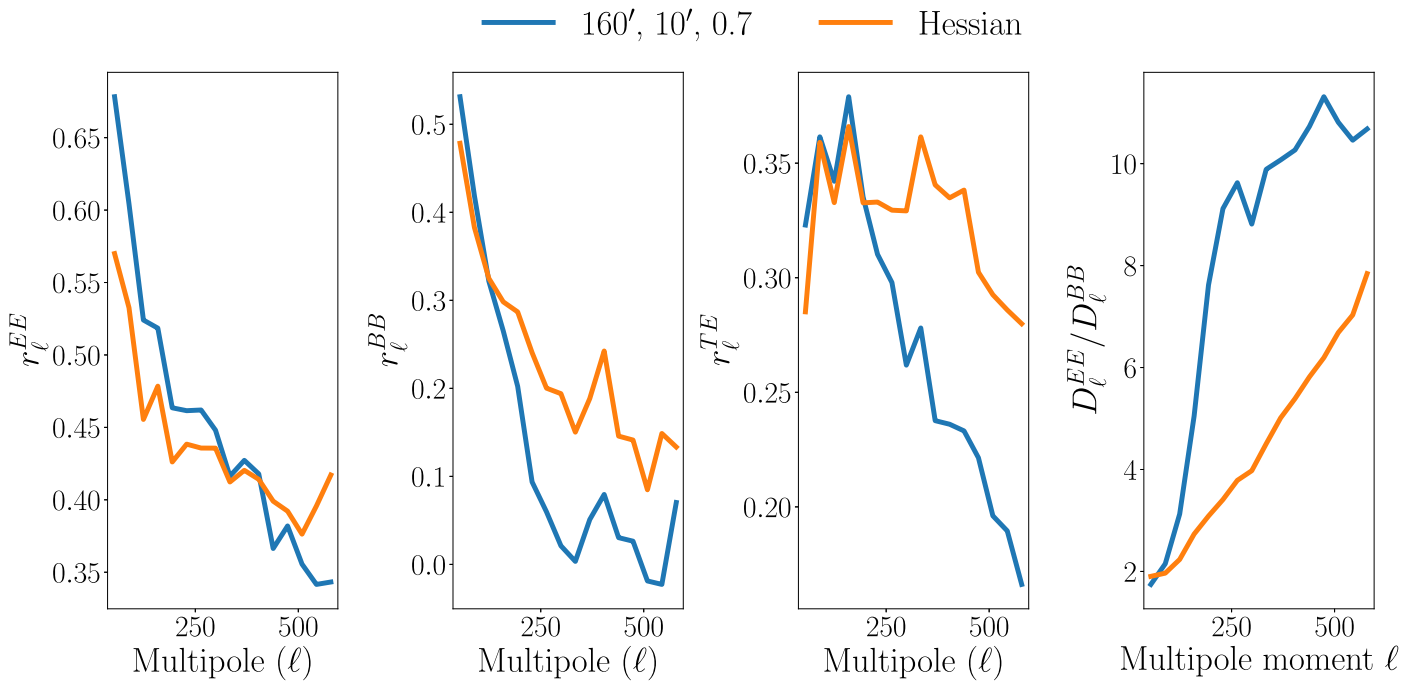

Figure 16. The *EE* (left), *BB* (middle left), and *TE* (middle right) correlation ratios of the Planck `Commander` dust maps with the H I-based polarization template constructed using the Hessian algorithm (orange) and those constructed using the Spherical RHT with $D_W = 160'$, $\theta_{FWHM} = 10'$, and $Z = 0.7$ (blue). The right panel shows the *EE*-to-*BB* ratios of the autospectra of the aforementioned H I-based polarization templates. All spectra in this figure are calculated using the Planck 70% sky fraction mask.

For the templates constructed with the Spherical RHT algorithm, the *EE*-to-*BB* autospectrum ratio peaks at different multipoles for different parameter sets, which determine the typical size of the measured filaments. The peaks are driven by the *EE* autospectra in the numerators of these ratios. This is because *E* modes predominantly originate along the filaments, so the most sensitive scale of the filament quantification method sets the dominant scale of the *E*-mode power. Note that these templates correctly predict an excess of *E* modes over *B* modes, supporting the idea that a preference for filaments in the real sky to be magnetically aligned results in an observed *EE*-to-*BB* ratio higher than unity (Clark et al. 2015; Planck Collaboration et al. 2016c). These templates, however, may overpredict the fraction of power in *E* modes on certain scales. Any method of quantifying filament orientations will be more or less sensitive to structure on particular scales (see the discussion in Hacar et al. 2022). This means that an H I-based polarization template built from filament orientations will have H I-based polarized intensity concentrated at particular angular scales, as is the case in this work. Some of the overprediction of *E* modes is likely due to this scale dependence not being representative of the hierarchical filamentary morphology of the real sky. Additionally, the H I-based polarization template may have excess *E*-mode power in part because they only model the filamentary component of the polarized dust emission, whereas the real sky contains additional polarized emission in extended structures that may not resemble filaments. The *BB*-to-*EE* ratio of the real polarized dust emission observed by Planck over large sky areas is $\sim 0.53 \pm 0.01$ over the multipole range $40 \leqslant \ell \leqslant 600$ (Planck Collaboration et al. 2020c).

Although we found that the Spherical RHT template correlates better with polarized dust emission than the Hessian template between $\ell = 20$ and $\ell = 140$, the Hessian algorithm correlates better at higher multipoles, especially in *B* modes, as shown in Figure 16. Because the RHT and Hessian templates predict different distributions of both polarization angles and polarized intensity, we investigate whether one of these factors is driving the stronger correlation between the Hessian-based template and the polarized dust emission data.

We implement a modification to the Spherical RHT–based template construction to make its orientation angle selection more similar to that of the Hessian algorithm. While the Hessian algorithm determines the orientation of the filaments based on the local eigenbasis, the H I-based polarization template constructed with the RHT algorithm computes a mean over all orientations weighted by the result of the convolutions at those orientations $R(\hat{\boldsymbol{n}}, \theta, \nu)$; (see Section 4). Therefore, we instead take the angle at the peak of $R(\hat{\boldsymbol{n}}, \theta, \nu)$ as the orientation of the filament. We find that for small window diameters D_W, this increases the *E*-mode correlation with the polarized dust emission by $\sim$5%. However, the effect is negligible in *B* modes and for large window diameters. This behavior is expected because larger window diameters are more likely to have singly peaked $R(\hat{\boldsymbol{n}}, \theta, \nu)$, such that the weighted mean of the angles and the angle at peak $R(\hat{\boldsymbol{n}}, \theta, \nu)$ are similar.

Each Stokes Q/U template is constructed from H I-based orientations and H I-based polarized intensity. We construct hybrid templates where the orientations are derived from the Spherical RHT and the polarized intensities are derived from the Hessian, and vice versa. Using the Spherical RHT parameters that produce the best correlation with the Hessian algorithm, we construct additional templates using Spherical RHT orientations, but weighting the Stokes *Q* and *U* maps by the Hessian eigenvalue-based weighting $w_H(\hat{\boldsymbol{n}}, \nu)$ described in Section 3.3 instead of the H I-intensity-based weighting $I_{H\,I}(\hat{\boldsymbol{n}}, \nu)$. Similarly, we construct another hybrid template using Hessian-derived orientations and Stokes *Q* and *U* maps weighted by the H I-

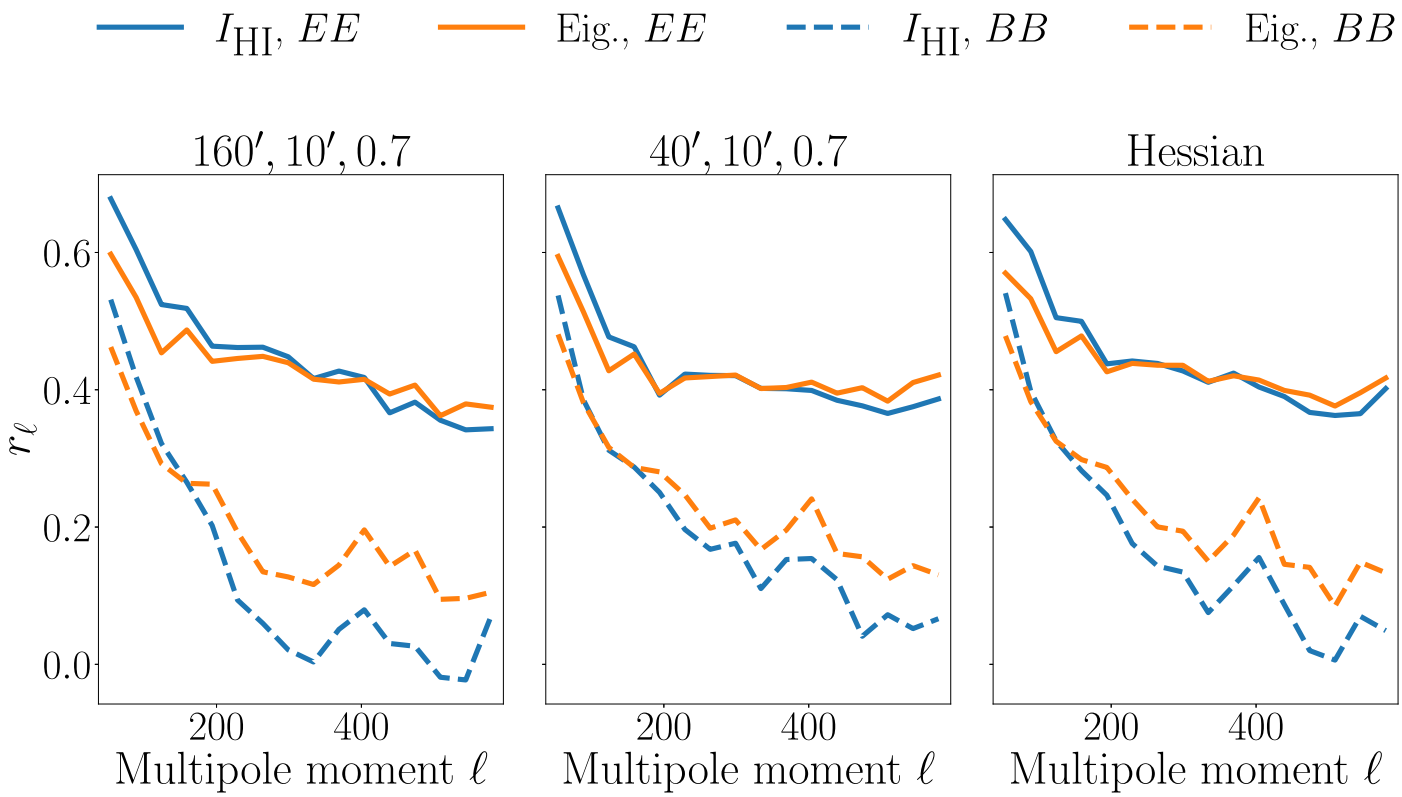

Figure 17. The *EE* (solid) and *BB* (dashed) correlation ratios of the Planck `Commander` dust maps with the H I-based polarization template constructed using different algorithms for the orientation angle calculations (different panels) and different weighting schemes (different colors). The left and middle panels use the Spherical RHT algorithm with different parameters for the orientation angle calculations, and the right panel uses the Hessian algorithm for those calculations. The parameters listed in the titles of the left and middle panels are the $D_{\rm W}$, $\theta_{\rm FWHM}$, and Z, respectively, defined in Section 3.1. In each panel, the H I intensity-based polarized intensity weighting (blue) is compared with the Hessian eigenvalue-based polarized intensity weighting (orange).

intensity-based weighting instead of the Hessian eigenvalue-based weighting. The main difference between the two polarized intensity weighting maps is that the Hessian eigenvalue-based one has a more uniform weighting across different filaments than the H I-intensity-based one. The standard deviation divided by the mean of the logarithm of the Hessian eigenvalue-based weighting maps is ∼0.1 and ∼0.25 for the H I-intensity-based one. Also, for a wide filament with relatively abrupt edges, the Hessian eigenvalue-based weighting upweights those edges relative to the rest of the filament. This is not the case for the H I-intensity-based weighting.

We compare the *EE* and *BB* correlation ratios with the Planck `Commander` dust maps of these hybrid maps compared to those of the maps constructed with the original polarized intensity weighting in Figure 17 to isolate the effect of the weighting scheme. We find that the Hessian eigenvalue-based weighting increases the correlation at higher multipoles. This is especially the case for *B* modes, where the improvement is at the level of ∼10%. The improvement is less obvious in *E* modes, especially when the Hessian algorithm is used for the orientation angle calculation. In Figure 17, we repeat the exercise with the set of parameters that we found in Figure 14 to maximize the correlation with the Hessian-based template and confirm the same qualitative conclusion. These results are not latitude dependent. They are also consistent with our results in Figure 16, where we see that the improvement in the *B*-mode correlation at small scales for the Hessian-based template over the Spherical RHT–based template is more obvious than the *E*-mode correlation. Therefore, we attribute most of the enhancement in the *B*-mode correlation of the template constructed using the Hessian algorithm to the polarized intensity weighting applied to the different filaments in the Stokes *Q* and *U* maps. This indicates that the relative weighting of the filaments relative to one another affects *B* modes more than it affects *E* modes. We correlate the weighting maps directly with the Planck `Commander` dust polarized emission. The correlation with the H I-intensity-based weighting map is stronger at large scales and weaker at small scales compared to the correlation with the Hessian eigenvalue-based weighting. This is consistent with the results for the H I-based polarization templates themselves.

7. Conclusions

We examine the impact of various alterations to H I-based polarization templates on the correlation with polarized millimeter-wave observations. This correlation probes the relationship between filamentary ISM structures and the magnetic field, and we investigate what H I structures are most predictive of the magnetic field orientation. We also use this framework to quantify the contribution of ISM filaments to the polarized dust emission power spectra. This is useful for CMB foreground separation. We make the H I-based polarization templates discussed in this work publicly available at doi:10.7910/DVN/74MEMX.

We summarize the conclusions of this work below.

1. We improve the *B*-mode correlation between the Hessian-based template and the polarized dust emission by ∼5% over that in Cukierman et al. (2023) by limiting the H I velocity range used to $-13\,{\rm km\,s^{-1}} < v_{\rm lsr} < 16\ {\rm km\,s^{-1}}$.

This is similar to the LVC range proposed in Panopoulou & Lenz (2020). The correlation with dust polarization is worse for wider velocity ranges when using the Hessian method because the Hessian is sensitive to artifacts in low-signal, high–absolute velocity channels.

2. We quantify the correlation between the Hessian-based template and the polarized dust emission in different masks of the sky and find it to be highest (at the ∼30%–60% level) in the region between the Planck 20% and 40% sky fraction masks and lowest (at the ∼10%–20% level) in the region that covers the 20% of the sky with the highest integrated dust intensity, i.e., the lowest Galactic latitudes.
3. We introduce the Spherical RHT algorithm, an efficient version of the RHT algorithm that uses spherical harmonic convolutions to run directly on the sphere. We find that the Spherical RHT fixes a spurious *EB* signal present at the ∼5% level in the Clark & Hensley (2019) H I-based polarization template due to projection effects.
4. We use the Spherical RHT to explore the parameter space of filament morphologies and their resulting polarization patterns. We find that the thinnest resolved H I filaments are the most informative for determining the magnetic field orientation. We also find that when using the Hessian method, the H I-based polarization template constructed from the GALFA-H I data smoothed to 7′ correlates ∼10% better with the *B*-mode polarized dust emission field than a template constructed from the 16′ HI4PI data. This motivates the use of even higher resolution H I data, such as the forthcoming Galactic Australian Square Kilometre Array Pathfinder (GASKAP; Dickey et al. 2013) and the Deep Synoptic Array (DSA-2000; Hallinan et al. 2019).
5. We use the Spherical RHT to demonstrate that parity-violating morphologies in the ISM can give rise to nonzero *TB* and *EB* even when local structures are perfectly aligned with the magnetic field. Since cosmic birefringence could lead to parity-odd polarization signals in the CMB, it is important to quantify parity-odd polarized dust emission as a foreground to those signals.
6. We apply the Spherical RHT to maps of synthetic filaments. We show how individual filament geometries mainly affect the *E*-mode pattern, whereas the positions and orientations of the filaments relative to one another mainly affect the *B*-mode pattern. We encourage the reader to use the Spherical RHT for exploring the polarization signatures of other synthetic filament morphologies.
7. We compare the Spherical RHT- and Hessian-based polarization templates. We find that the most significant difference in the correlation with polarized dust emission is in *B* modes at small scales, where the Hessian-based template produces a higher correlation. We find that this is due to the difference in the polarized intensity weightings of the templates. The Spherical RHT–based template uses the H I intensity distribution, while the Hessian-based template uses the Hessian eigenvalue map, which tends to be more uniform. This indicates that *B* modes are more sensitive to the polarized intensity weighting of different filaments relative to one another than *E* modes are.

The correlation ratio between the integrated HI4PI intensity map and the Planck total intensity map at 353 GHz over the Planck 70% sky fraction Galactic plane mask decreases from ∼80% at $\ell \sim 40$ to ∼35% at $\ell \sim 600$ (Cukierman et al. 2023). This imperfect correlation is partly due to the cosmic infrared background (CIB) in the Planck total intensity map, as well as uncorrelated data noise and systematics. The correlation between the H I-based polarization templates and the dust polarization in *EE* decreases from ∼60% at $\ell \sim 40$ to ∼45% at $\ell \sim 600$. The strength of this correlation is partly affected by the fact that the H I-based polarization templates do not quantify the diffuse, non-filamentary component of the dust, nor the small local misalignments between the orientations of filaments and magnetic fields.

In addition to providing intuition on the filamentary polarized dust emission patterns, these conclusions provide a step forward in modeling dust polarization using H I data. This work has focused on comparisons to the observed polarized dust emission using polarization power spectra. Future work could consider additional metrics, including those sensitive to non-Gaussian structures in the dust, e.g., Minkowski functionals (Mantz et al. 2008) or the scattering transform (Mallat 2011). These techniques have recently been used to quantify structures in dust (Delouis et al. 2022) and in H I emission (Lei & Clark 2023) individually.

Acknowledgments

This work was supported by the National Science Foundation under grant No. AST-2106607 (PI S.E.C.).

This publication utilizes data from Planck, an ESA science mission funded by ESA Member States, NASA, and Canada.

This work makes use of data from the HI4PI Survey, which is constructed from the Effelsberg–Bonn H I Survey (EBHIS), made with the 100 m radio telescope of the MPIfR at Effelsberg/Germany, and the Galactic All-Sky Survey (GASS), observed with the Parkes Radio Telescope, part of the Australia Telescope National Facility, which is funded by the Australian Government for operation as a National Facility managed by CSIRO. EBHIS was funded by the Deutsche Forschungsgemein-schaft (DFG) under the grants KE757/7-1 to 7–3.

This work makes use of data from the Galactic Arecibo *L*-band Feed Array H I (GALFA-H I) Survey. It is with the Arecibo 305 m telescope, which is operated by SRI International under a cooperative agreement with the National Science Foundation (AST-1100968), and in alliance with Ana G. Méndez-Universidad Metropolitana and the Universities Space Research Association. The GALFA-H I surveys have been funded by the NSF through grants to Columbia University, the University of Wisconsin, and the University of California.

The computations in this paper were run on the Sherlock cluster, supported by the Stanford Research Computing Center at Stanford University.

Software: astropy (Astropy Collaboration et al. 2013, 2018, 2022), Healpix[9] (Górski et al. 2005), healpy (Zonca et al. 2019), matplotlib (Hunter 2007), numpy (Oliphant 2015), scipy (Virtanen et al. 2020), ducc,[10] pspy[11] (Louis et al. 2020).

ORCID iDs

George Halal https://orcid.org/0000-0003-2221-3018
Susan E. Clark https://orcid.org/0000-0002-7633-3376
Ari Cukierman https://orcid.org/0000-0002-7471-719X
Dominic Beck https://orcid.org/0000-0003-0848-2756

[9] http://healpix.sourceforge.net/
[10] https://gitlab.mpcdf.mpg.de/mtr/ducc
[11] https://github.com/simonsobs/pspy

References

Abitbol, M. H., Hill, J. C., & Johnson, B. R. 2016, MNRAS, 457, 1796
Astropy Collaboration, Price-Whelan, A. M., Lim, P. L., et al. 2022, ApJ, 935, 167
Astropy Collaboration, Price-Whelan, A. M., Sipőcz, B. M., et al. 2018, AJ, 156, 123
Astropy Collaboration, Robitaille, T. P., Tollerud, E. J., et al. 2013, A&A, 558, A33
BICEP/Keck Collaboration, Ade, P. A. R., Ahmed, Z., et al. 2023, ApJ, 945, 72
Boe, B., Habbal, S., & Druckmüller, M. 2020, ApJ, 895, 123
Boulanger, F., Abergel, A., Bernard, J. P., et al. 1996, A&A, 312, 256
Carrière, J. S., Ferrière, K., Ristorcelli, I., & Montier, L. 2022, A&A, 668, A42
Challinor, A., Fosalba, P., Mortlock, D., et al. 2000, PhRvD, 62, 123002
Chiang, Y.-K., & Ménard, B. 2019, ApJ, 870, 120
Clark, S. E. 2018, ApJL, 857, L10
Clark, S. E., & Hensley, B. S. 2019, ApJ, 887, 136
Clark, S. E., Hill, J. C., Peek, J. E. G., Putman, M. E., & Babler, B. L. 2015, PhRvL, 115, 241302
Clark, S. E., Kim, C.-G., Hill, J. C., & Hensley, B. S. 2021, ApJ, 919, 53
Clark, S. E., Peek, J., Putman, M., Schudel, L., & Jaspers, R., 2020 RHT: Rolling Hough Transform, Astrophysics Source Code Library, ascl:2003.005
Clark, S. E., Peek, J. E. G., & Putman, M. E. 2014, ApJ, 789, 82
Colombi, S., Pogosyan, D., & Souradeep, T. 2000, PhRvL, 85, 5515
Cukierman, A. J., Clark, S. E., & Halal, G. 2023, ApJ, 946, 106
Delouis, J. M., Allys, E., Gauvrit, E., & Boulanger, F. 2022, A&A, 668, A122
Dickey, J. M., McClure-Griffiths, N., Gibson, S. J., et al. 2013, PASA, 30, e003
Forero-Romero, J. E., Hoffman, Y., Gottlöber, S., Klypin, A., & Yepes, G. 2009, MNRAS, 396, 1815
Górski, K. M., Hivon, E., Banday, A. J., et al. 2005, ApJ, 622, 759
Hacar, A., Clark, S., Heitsch, F., et al. 2022, in ASP Conf. Ser. 534, Protostars and Planets VII, ed. S.-i. Inutsuka et al. (San Francisco, CA: ASP), 153
Halal, G., Clark, S. E., Cukierman, A., Beck, D., & Kuo, C.-L. 2023, Spherical Rolling Hough Transform, v2.0.1, Zenodo, doi:10.5281/zenodo.8025777
Hallinan, G., Ravi, V., Weinreb, S., et al. 2019, BAAS, 51, 255
Han, J. L. 2017, ARA&A, 55, 111
HI4PI Collaboration, Ben Bekhti, N., Flöer, L., et al. 2016, A&A, 594, A116
Hough, P. V. 1962, Method and Means for Recognizing Complex Patterns, US Patent 3.069.654, https://www.osti.gov/biblio/4746348
Huffenberger, K. M., Rotti, A., & Collins, D. C. 2020, ApJ, 899, 31
Hunter, J. D. 2007, CSE, 9, 90
Inoue, T., & Inutsuka, S.-i. 2016, ApJ, 833, 10
Jelić, V., Prelogović, D., Haverkorn, M., Remeijn, J., & Klindžić, D. 2018, A&A, 615, L3
Kalberla, P. M. W., Burton, W. B., Hartmann, D., et al. 2005, A&A, 440, 775
Kalberla, P. M. W., Kerp, J., & Haud, U. 2021, A&A, 654, A91
Kamionkowski, M., Kosowsky, A., & Stebbins, A. 1997, PhRvL, 78, 2058
Lei, M., & Clark, S. E. 2023, ApJ, 947, 74
Lenz, D., Hensley, B. S., & Doré, O. 2017, ApJ, 846, 38
Louis, T., Naess, S., Garrido, X., & Challinor, A. 2020, PhRvD, 102, 123538
Malinen, J., Montier, L., Montillaud, J., et al. 2016, MNRAS, 460, 1934
Mallat, S. 2011, arXiv:1101.2286
Mantz, H., Jacobs, K., & Mecke, K. 2008, JSMTE, 2008, 12015
McClure-Griffiths, N. M., Pisano, D. J., Calabretta, M. R., et al. 2009, ApJS, 181, 398
Minami, Y., & Komatsu, E. 2020, PhRvL, 125, 221301
Oliphant, T. E. 2015, Guide to NumPy (2nd ed.; North Charleston, SC: CreateSpace Independent Publishing Platform)
Panopoulou, G. V., & Lenz, D. 2020, ApJ, 902, 120
Panopoulou, G. V., Psaradaki, I., & Tassis, K. 2016, MNRAS, 462, 1517
Panopoulou, G. V., Tassis, K., Skalidis, R., et al. 2019, ApJ, 872, 56
Pearson, S., Clark, S. E., Demirjian, A. J., et al. 2022, ApJ, 926, 166
Peek, J. E. G., Babler, B. L., Zheng, Y., et al. 2018, ApJS, 234, 2
Pelgrims, V., Clark, S. E., Hensley, B. S., et al. 2021, A&A, 647, A16
Polychroni, D., Schisano, E., Elia, D., et al. 2013, ApJL, 777, L33
Prézeau, G., & Reinecke, M. 2010, ApJS, 190, 267
Planck Collaboration, Abergel, A., Ade, P. A. R., et al. 2011, A&A, 536, A24
Planck Collaboration, Ade, P. A. R., Aghanim, N., et al. 2015, A&A, 576, A104
Planck Collaboration, Adam, R., Ade, P. A. R., et al. 2016a, A&A, 594, A10
Planck Collaboration, Adam, R., Ade, P. A. R., et al. 2016b, A&A, 586, A135
Planck Collaboration, Ade, P. A. R., Aghanim, N., et al. 2016c, A&A, 586, A141
Planck Collaboration, Akrami, Y., Ashdown, M., et al. 2020a, A&A, 641, A4
Planck Collaboration, Aghanim, N., Akrami, Y., et al. 2020b, A&A, 641, A1
Planck Collaboration, Akrami, Y., Ashdown, M., et al. 2020c, A&A, 641, A11
Purcell, E. M. 1975, The Dusty Universe (New York: Neale Watson Academic Publications, Inc.), 155
Raymond, J. C., Slavin, J. D., Blair, W. P., et al. 2020, ApJ, 903, 2
Seljak, U. 1997, ApJ, 482, 6
Seljak, U., & Zaldarriaga, M. 1997, PhRvL, 78, 2054
Virtanen, P., Gommers, R., Oliphant, T. E., et al. 2020, NatMe, 17, 261
Wakker, B. P., & Boulanger, F. 1986, A&A, 170, 84
Wandelt, B. D., & Górski, K. M. 2001, PhRvD, 63, 123002
Winkel, B., Kerp, J., Flöer, L., et al. 2016, A&A, 585, A41
Zaldarriaga, M. 2001, PhRvD, 64, 103001
Zonca, A., Singer, L., Lenz, D., et al. 2019, JOSS, 4, 1298